Nanoscale
Advances

PAPER

View Article Online
View Journal | View Issue

Cite this: *Nanoscale Adv.*, 2025, 7, 6032

Fabrication of TiO_2@SnS_2 core–shell nanocomposites *via* a thermal decomposition approach for sunlight-driven photodegradation of crystal violet

Nainy Khera and Jeevanandam Pethaiyan *

In the current study, TiO_2@SnS_2 core–shell nanocomposites were prepared *via* a facile thermal decomposition method. The synthesis consists of thermal decomposition of tin chloride pentahydrate and thiourea in the presence of NaOH-modified TiO_2 microspheres in diphenyl ether (DPE) at ∼200 °C in air. The synthesized TiO_2@SnS_2 core–shell nanocomposites were characterized by XRD, FT-IR, TGA, FESEM, TEM, EDXA, UV-DRS, PL and XPS. The XRD results indicate the presence of both TiO_2 and SnS_2 phases in the core–shell nanocomposites. FESEM, TEM and EDX analyses results confirm uniform coating of SnS_2 nanoparticles on the surface modified TiO_2 microspheres. XPS analysis results confirm the presence of Sn^{4+}, Ti^{4+}, O^{2-} and S^{2-} in the TiO_2@SnS_2 nanocomposites. After their characterization, the TiO_2@SnS_2 core–shell nanocomposites were explored for their catalytic activity towards the photodegradation of a toxic dye (crystal violet (CV)) in an aqueous solution under sunlight. The photodegradation efficiency of TiO_2@SnS_2 core–shell nanocomposites is better than that of TiO_2 microspheres, SnS_2 nanoparticles and other metal sulfide nanoparticles/nanocomposites reported in the literature.

Received 31st May 2025
Accepted 1st August 2025

DOI: 10.1039/d5na00533g

rsc.li/nanoscale-advances

1 Introduction

Water pollution from dyes threatens ecosystems across the globe. As human population and economies expand, water pollution has become one of the major issues. The unavailability of sufficient freshwater not only affects human life but it also affects biodiversity and other ecosystems.[1] Textile industries produce organic contaminants such as synthetic dyes in high amounts. The dyes do not bind tightly to the fabric and about 20% of them are discharged without any prior treatment into water systems and cause pollution.[2] The toxic dyes are often stable, carcinogenic and poisonous.[3] In the past few decades, scientists have been working on different methods for the treatment of contaminated water. Photocatalysis is widely explored for the degradation of toxic dyes. It has advantages such as use of sunlight, low cost and being an environment friendly process.[4]

Photocatalysts based on metal oxide nanoparticles such as TiO_2,[5] MoO_{3-x},[6] Cu_2O,[7] WO_3,[8] and $NiCo_2O_4$,[9] and metal sulfide nanoparticles such as NiS,[10] MoS_2,[11] CuS,[12] and SnS_2 [13] have been explored as catalysts for the degradation of toxic dyes. Several core–shell nanocomposites such as CuS/ZnO,[14] ZnO@ZnS,[15] $CoFe_2O_4$@$CoWO_4$,[16] MoO_3@MoS_2,[17] CdS@ZnO,[18] TiO_2@$CoFe_3O_4$,[19] WO_3@TiO_2,[20] $ZnIn_2S_4$@CeO_2,[21] ZnO@SnS_2,[22] and α-Fe_2O_3@SnO_2/Ti_3C_2 [23] have been explored for the photodegradation of dyes such as methylene blue, congo red, rhodamine B, methyl orange, malachite green, *etc.* and they show better activity than pure metal sulfide and metal oxide nanoparticles.

Different SnS_2 based nanocomposites are reported in the literature such as SnS_2/chitosan, synthesized *via* the precipitation method, for photodegradation of crystal violet,[24] SnS_2/biochar nanocomposite, synthesized *via* the hydrothermal route, for photodegradation of amoxycillin and congo red,[25] SnS_2/$BiVO_4$ nanocomposite, synthesized *via* the hydrothermal route, for photocatalytic degradation of ciprofloxacin,[26] SnS_2/CdO nanocomposite, synthesized *via* the precipitation method, for photodegradation of RhB and congo red,[27] SnS_2/Ag_3VO_4 nanocomposite, synthesized *via* the hydrothermal method, for photodegradation of methylene blue,[28] SnS_2/NiCo-LDH nanocomposite, synthesized *via* the co-precipitation method, for photodegradation of thiamethoxam,[29] polyaniline/SnS_2 nanocomposite, synthesized by the hydrothermal method, for hydrogen evolution,[30] PVDF/SnS_2 nanocomposite, synthesized *via* the hydrothermal method, for piezoelectric energy harvesting,[31] CeO_2/SnS_2/polyaniline nanocomposite, synthesized *via* the hydrothermal method, for photocatalytic reduction of Cr(VI),[32] PbS : SnS_2 nanocomposite, synthesized *via* the precipitation method, for ethanol sensing,[33] Pd/SnS_2/SnO_2

Department of Chemistry, Indian Institute of Technology Roorkee, Roorkee-247667, India. E-mail: jeevafcy@iitr.ac.in; Fax: +91-1332-273560; Tel: +91-1332-285444

nanocomposite, synthesized *via* the hydrothermal method, for detection of H_2,[34] Au/SnS_2 nanocomposite, synthesized *via* chemical reduction method, as a NO_2 gas sensor,[35] MoS_2/SnS_2 nanocomposite, synthesized *via* the hydrothermal method, as an anode in sodium ion batteries,[36] SnS_2/CuO nanocomposite, synthesized by the precipitation method, in broadband photodetectors,[37] BiOI@SnS_2 core–shell nanocomposite, synthesized *via* the co-precipitation method, for photodegradation of RhB,[38] and $MnFe_2O_4$@SnS_2 core–shell nanocomposite, synthesized *via* the hydrothermal method, for photodegradation of methylene blue.[39]

TiO_2 is a semiconductor with a wide band gap (E_g (bulk) = 3.2 eV).[40] It is a well-known semiconductor for environmental remediation and it exhibits high recombination of photogenerated electrons and holes leading to its low photocatalytic activity. SnS_2 is economical and non-toxic with good thermal stability.[41,42] It has a narrow band gap of about 1.9 eV [43] and is known to exhibit good photocatalytic activity.[42,44] To improve the photocatalytic activity of TiO_2 further, formation of a nanocomposite of TiO_2 with SnS_2 has been proposed. Both the valence band (VB) and conduction band (CB) of SnS_2 lie below those of TiO_2. Due to this, during light irradiation, the photogenerated electrons from the CB of SnS_2 are easily transferred to that of TiO_2. This enhances the separation of electrons and holes and improves the photocatalytic efficiency.[45] TiO_2–SnS_2 nanocomposites are useful for various applications such as photodegradation of dyes such as methyl orange, methylene blue and RhB,[46–48] photodegradation of antibiotics such as tetracycline,[49] NO_2 gas sensors,[50,51] humidity sensors,[52,53] protection of stainless steel,[54] photodetectors,[55] H_2 gas production,[56,57] biosensors,[58] photoreduction of Cr(VI),[45] photocatalytic H_2 evolution,[59] anode material in lithium-ion batteries,[60] photodegradation of diclofenac,[61] self-decontaminating textiles,[62] photoelectrochemical water splitting,[63] photodegradation of diethyl sulfide,[64] electrocatalytic oxygen evolution,[65] and photocatalytic reduction of CO_2.[66]

In the current study, TiO_2@SnS_2 core–shell nanocomposites have been synthesized. The novelty of this work is as follows. In the literature, TiO_2–SnS_2 nanocomposites have been reported (*e.g.*, yolk–shell SnS_2–TiO_2 microsphere composite[67] and SnS_2@TiO_2 double shell nanocomposite[47]) but the core–shell structure of the nanocomposite (TiO_2@SnS_2) has not been previously reported. The thermal decomposition method has been used for the synthesis of different metal sulfide nanoparticles and their nanocomposites. However, the synthesis of a TiO_2@SnS_2 nanocomposite has not been previously reported using this approach. The reported methods used for the synthesis of TiO_2–SnS_2 nanocomposites in the literature (solvothermal,[50] hydrothermal,[52] chemical bath deposition,[55] and sol–gel method[61]) have disadvantages such as use of high pressure (50 bar to 2 kbar) and prolonged reaction time (12 h to 16 h). For example, the sol–gel method requires a reaction time of up to 7 days, and the chemical bath deposition method is a two-step process and often requires an inert environment. The current study reports the synthesis of TiO_2@SnS_2 core–shell nanocomposites using a thermal decomposition method with a shorter synthesis time (60 min) without the need of an inert environment. The TiO_2@SnS_2 core–shell nanocomposites were first characterized using various techniques and then they were explored for their photocatalytic activity towards the photodegradation of CV.

2 Experimental

2.1 Materials

Titanium isopropoxide (TIP) (97%, Sigma-Aldrich), $SnCl_4 \cdot 5H_2O$ (98%, Sigma-Aldrich), thiourea (98%, SRL Chemicals), methanol (MeOH) (99%, Rankem), acetonitrile (99.5%, Rankem), dodecylamine (DDA) (99%, Rankem), sodium hydroxide (99%, Rankem), diphenyl ether (DPE, 99%, Sigma-Aldrich) and crystal violet (CV, 97%, Sigma-Aldrich) were used.

2.2 Preparation of materials

2.2.1 Synthesis of TiO_2 microspheres. TiO_2 microspheres were prepared using a reported wet chemical method.[68] Typically, 0.18 mL of H_2O and 0.345 mL of dodecyl amine (DDA) were taken in a mixture of solvents (100 mL of methanol and 50 mL of acetonitrile) and the contents were stirred for 10 min. After this, 1 mL of titanium isopropoxide was added and the reaction mixture was further stirred for about 6 h at room temperature. The contents were centrifuged, and the collected product was washed with MeOH and dried in an oven at 60 °C for 12 h to obtain as-prepared TiO_2 microspheres. Dodecylamine acts as a surfactant during the synthesis of TiO_2 microspheres. Its hydrophilic amine group interacts with polar solvent molecules (methanol), while the hydrophobic tail interacts with non-polar titanium isopropoxide. During the hydrolysis and condensation of TIP, it forms TiO_2 nuclei. The hydrophobic tail of DDA binds to TiO_2 particles *via* van der Waals forces preventing agglomeration. This stabilizes the dispersion, lowers surface energy, and leads to controlled nucleation and growth, resulting in uniform TiO_2 microspheres.[69,70] The as-prepared TiO_2 microspheres were calcined at 500 °C for 3 h (heating rate = $2° \text{ min}^{-1}$) to obtain calcined TiO_2 microspheres. The calcined TiO_2 microspheres were surface-modified using NaOH.[71] For this, 100 mg of calcined TiO_2 microspheres were added to 10 mL of 5 M NaOH aqueous solution and left at room temperature for about 24 h. The contents were centrifuged, washed with de-ionised water and with 0.1 N HCl solution. The sample was dried in an oven at 60 ° C for 12 h to obtain NaOH-modified TiO_2 microspheres (TiO_2–NaOH).

Zeta potential measurements were done for calcined TiO_2 and NaOH-modified TiO_2. The surface charge as measured from the zeta potential analyzer was +10.1 mV and −11.8 mV for TiO_2-calc. and TiO_2–NaOH, respectively. The change in surface charge from positive to negative indicates successful surface modification of TiO_2 microspheres with NaOH.

2.2.2 Synthesis of TiO_2@SnS_2 core–shell nanocomposites. To synthesize TiO_2@SnS_2 core–shell nanocomposites, 100 mg of TiO_2–NaOH microspheres were taken in 10 mL of DPE in a 50 mL RB flask. The contents were sonicated for one min followed by addition of x mmol of $SnCl_4 \cdot 5H_2O$ and $2x$ mmol of

Table 1 Synthetic details of TiO_2@SnS_2 core–shell nanocomposites and their sample codes

Sample code	TiO_2–NaOH (mg)	$SnCl_4\cdot 5H_2O$ (mmol)	Thiourea (mmol)	Solvent	Reaction temperature (°C)	Reaction time (min)
SnS_2	—	0.50	1.0	Diphenyl ether	200 ± 2	60 ± 5
TiO_2–SnS_2-0.05	100	0.05	0.1	Diphenyl ether	200 ± 2	60 ± 5
TiO_2–SnS_2-0.1	100	0.10	0.2	Diphenyl ether	200 ± 2	60 ± 5
TiO_2–SnS_2-0.15	100	0.15	0.3	Diphenyl ether	200 ± 2	60 ± 5

thiourea (Table 1). After refluxing the reaction mixture for about 60 min in air at about 200 °C, the contents were allowed to cool to RT, followed by the addition of about 20 mL of MeOH. The obtained brown precipitate was centrifuged and washed (2–3 times) with methanol. The precipitate was dried in a vacuum desiccator overnight to obtain the TiO_2@SnS_2 core–shell nanocomposite. Pure SnS_2 nanoparticles were also synthesized using a similar synthetic approach in the absence of TiO_2–NaOH microspheres.

2.3 Photocatalytic studies

Crystal violet is toxic and carcinogenic with a complex structure and is widely used in textiles, microbiological staining, printing, *etc.*, and leads to water pollution. CV is a cationic triphenylmethane dye which is highly resistant to natural degradation.

All the photodegradation experiments were done under sunlight irradiation between 1 PM and 2 PM at Indian Institute of Technology Roorkee, Roorkee, India between March 2024 and May 2024. The solar irradiance data were obtained using the average solar data sourced from ProfileSolar.[72] The average intensity of the sun during spring (March–May) is about 6.62 kWh per m^2 per day, *i.e.*, 276 W m^{-2} h^{-1}. The photocatalytic experiments were done by taking 5 mg each of TiO_2@SnS_2 core–shell nanocomposites in 5 mL of CV aqueous solution (2×10^{-5} M) in a test tube followed by sonication for one minute. The adsorption–desorption equilibrium was achieved by keeping the mixture in the dark for about 30 min. After that, the contents were exposed to sunlight for 60 min. The contents were centrifuged to remove the photocatalyst and the supernatant solutions were analysed using UV-Vis spectroscopy. A blank experiment (*i.e.*, no catalyst) was also carried out to understand the self-degradation of crystal violet under sunlight. The % degradation of crystal violet was estimated using the following formula:

$$\text{Degradation\%} = (1 - C_t/C_0) \times 100$$

where C_0 and C_t denote the concentration of crystal violet at adsorption equilibrium and at any irradiation time 't', respectively.

2.4 Characterization

Powder X-ray diffraction (XRD) measurements were carried out for phase identification using a Rigaku Miniflex 600 powder X-ray diffractometer (Cu-K_α, $\lambda = 1.5406$ Å). A Thermo Nicolet FT-IR spectrophotometer was used for recording FT-IR spectra of the samples in the range of 4000–400 cm^{-1} using KBr pellets. For thermogravimetric analysis (TGA), a PerkinElmer Pyris Diamond instrument was employed in the temperature range of 30–1000 °C (heating rate = 10 °C min^{-1}) in air. The morphological and EDX analyses of the samples were done using a Thermofisher Apreo field emission SEM (operating voltage = 20 kV). TEM measurements were done using a Thermofisher TALOS F200X transmission electron microscope (operating voltage = 200 kV). For the TEM analysis, 1 mg of each sample was taken in a test tube to which 5 mL of ethanol was added. The mixture was sonicated for about 45 min and then drop-cast over a copper grid followed by drying overnight at room temperature. HRTEM images and SAED patterns of the nanocomposites were recorded using the same instrument. EDS line scan and elemental mapping of the nanocomposites were recorded using a JEOL JEM-3200FS transmission electron microscope (operating voltage = 300 kV; energy resolution = 127 eV). The measurements were performed by carefully optimizing the acquisition parameters, such as beam current and dwell time, to minimize beam effects and no significant beam-induced sample damage was observed during the EDS measurements. The oxidation states of the elements present in the TiO_2@SnS_2 core–shell nanocomposites were determined using a Physical Electronics PHI 5000 Versa Probe III XPS spectrometer using Al-Kα radiation ($\lambda = 1486.6$ eV). The optical studies on the core–shell nanocomposites were done using a Cary 5000 UV-Vis-NIR spectrophotometer in the reflectance mode in the wavelength range 300 nm to 800 nm. A diffuse reflectance accessory was used for this purpose. About 10 mg of each sample powder was used to measure the reflectance spectra. The specific surface area of the samples was measured *via* N_2 physisorption at 77 K on a Nova 2200e Quantachrome instrument using the BET method. A Shimadzu UV-2600 UV-Vis spectrophotometer was used for recording absorption spectra during the photodegradation studies. Photoluminescence (PL) spectral measurements were made using a Fluoromax-4 spectrofluorometer at room temperature. 1 mg of sample powder was dispersed in about 3 mL of deionized water by sonication and PL spectra were recorded for the dispersion with an excitation wavelength of 450 nm.

3 Results and discussion

3.1 X-ray diffraction

The powder XRD patterns of calcined TiO_2 (before NaOH modification) and TiO_2 (after modification with NaOH) are displayed in Fig. S1. The XRD patterns of both the samples show peaks at similar 2θ values and match with that of anatase TiO_2 (JCPDS file no. 84-1286) indicating that there is no change in the TiO_2 phase after modification with NaOH. The XRD patterns of TiO_2–NaOH, SnS_2 nanoparticles and TiO_2@SnS_2 core–shell nanocomposites are displayed in Fig. 1. The XRD pattern of TiO_2–NaOH microspheres shows peaks at $2\theta = 25.39°$, 36.96°, 37.93°, 38.76°, 48.02°, 53.94°, 55.19°, 62.74°, 68.93°, 70.39°, 75.14° and 76.2° which correspond to (101), (103), (004), (112), (200), (105), (211), (204), (116), (220), (215) and (301) planes, respectively, of the anatase phase of TiO_2. The XRD pattern of SnS_2 nanoparticles shows peaks at $2\theta = 28.32°$, 32.16°, 41.83°, 45.94°, 50.04°, 52.51°, 58.48°, 60.76°, 63.05°, 67.30° and 70.48° indexed to (100), (011), (012), (003), (110), (111), (200), (201), (004), (202) and (113) planes, respectively, of the Berndtite-2T phase of hexagonal SnS_2 (JCPDS file no. 83-1705). The powder XRD patterns of TiO_2@SnS_2 core–shell nanocomposites (TiO_2–SnS_2-0.05, TiO_2–SnS_2-0.1 and TiO_2–SnS_2-0.15) show peaks due to the anatase phase of TiO_2 and also show peaks at $2\theta = 28.59°$ and 50.35° due to (100) and (110) planes of the Berndtite-2T phase of hexagonal SnS_2. It is known that the crystallite coherence and stacking faults of nanoparticles may influence the activity.[73] The crystallite size of SnS_2 nanoparticles was estimated from the XRD patterns of SnS_2, TiO_2–SnS_2-0.05, TiO_2–SnS_2-0.1 and TiO_2–SnS_2-0.15 and the values are 11.6 nm, 10.2 nm, 8.8 nm and 8.4 nm, respectively. The crystallite size of TiO_2 was estimated from the XRD patterns of TiO_2–NaOH, TiO_2–SnS_2-0.05, TiO_2–SnS_2-0.1, and TiO_2–SnS_2-0.15 and the values are 16.2 nm, 15.9 nm, 15.1 nm, and 14.4 nm, respectively.

The dislocation density and crystallite strain for TiO_2 and SnS_2 were estimated for the TiO_2@SnS_2 core–shell nanocomposites. Dislocation density (ρ) is defined as the number of dislocation lines per unit volume and is estimated using eqn. (1).[74]

$$\rho = (1/D^2) \tag{1}$$

where D is the crystallite size.

The dislocation density values for SnS_2 in SnS_2, TiO_2–SnS_2-0.05, TiO_2–SnS_2-0.1 and TiO_2–SnS_2-0.15 are 0.0074 nm^{-2}, 0.0096 nm^{-2}, 0.0129 nm^{-2}, and 0.014 nm^{-2}, respectively. The dislocation density values for TiO_2 in TiO_2–NaOH, TiO_2–SnS_2-0.05, TiO_2–SnS_2-0.1 and TiO_2–SnS_2-0.15 are 0.0038 nm^{-2}, 0.0039 nm^{-2}, 0.0043 nm^{-2}, and 0.0048 nm^{-2}, respectively. The dislocation density of both TiO_2 and SnS_2 lattices is small. This suggests a high degree of crystallinity of TiO_2–NaOH, SnS_2, and TiO_2@SnS_2 core–shell nanocomposites. Also, the dislocation density increases as the thickness of the shell in the core–shell nanocomposites increases. Crystallite strain is defined as the small distortion in the crystal lattice due to defects or dislocations, causing a slight variation in atomic positions. Due to this, broadening of XRD peaks is observed without change in peak positions. The crystallite strain was estimated using eqn. (2).[75]

$$\beta \cos\theta = K\lambda/D + 4\varepsilon \sin\theta \tag{2}$$

where ε is the crystallite strain (or microstrain) and is determined from the slope of linear fit of the plot between $\beta \cos\theta$ and $4 \sin\theta$, commonly known as the Williamson–Hall plot. Fig. S2 provides the Williamson–Hall plots for TiO_2–NaOH and TiO_2@SnS_2 core–shell nanocomposites. The crystallite strain (ε) values for TiO_2–NaOH, TiO_2–SnS_2-0.05, TiO_2–SnS_2-0.1 and TiO_2–SnS_2-0.15 are 0.00378, 0.00395, 0.00432, and 0.00468, respectively. There is an increase in crystallite strain as shell (SnS_2) thickness increases. The presence of more number of dislocation lines/defects (dislocation density) leads to higher microstrain in the lattice.[76,77] The crystallite strain for SnS_2 could not be estimated as there are only two peaks due to SnS_2 in the XRD patterns of TiO_2@SnS_2 core–shell nanocomposites.

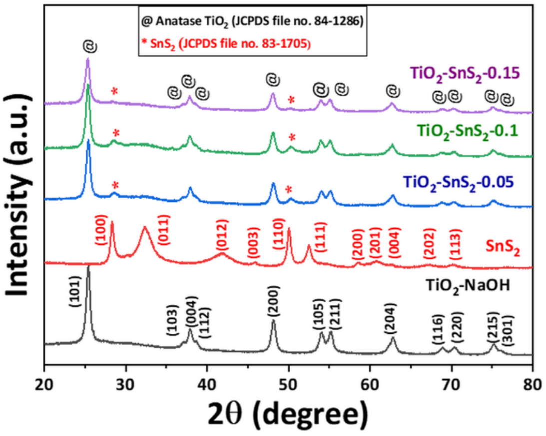

Fig. 1 XRD patterns of TiO_2–NaOH, SnS_2 nanoparticles and TiO_2@SnS_2 core–shell nanocomposites.

The TiO_2 microspheres (as prepared) were calcined at 750 °C and XRD analysis of the sample was performed to confirm the phase of TiO_2. The XRD pattern of TiO_2 calcined at 500 °C matches with the anatase phase of TiO_2 (JCPDS file no. 84-1286) whereas the XRD pattern of TiO_2 calcined at 750 °C matches with the rutile phase of TiO_2 (JCPDS file no. 04-0551) (Fig. S3). This indicates that phase transformation of TiO_2 from anatase into rutile takes place between 650 °C and 800 °C.

3.2 Functional group analysis

The FT-IR spectra of unmodified calcined TiO_2 microspheres and TiO_2–NaOH are given in Fig. S4. The intensities of IR bands due to OH stretching and bending are more intense in the case of TiO_2–NaOH microspheres compared to unmodified TiO_2 indicating the successful modification of calcined TiO_2 microspheres with NaOH. The FT-IR spectra of TiO_2–NaOH, SnS_2 nanoparticles, and TiO_2@SnS_2 core–shell nanocomposites are displayed in Fig. S5. The IR band positions and their assignments for all the samples are given in Table S1. The IR spectrum of TiO_2–NaOH microspheres shows bands at 3428 cm^{-1} and 1637 cm^{-1} due to the stretching and bending vibration of physisorbed water molecules.[78] The characteristic band due to Ti–O vibration is observed at about 624 cm^{-1}.[79] The IR spectra of SnS_2 nanoparticles and TiO_2@SnS_2 core–shell nanocomposites show vibrational bands at about 3397 cm^{-1} and 1638 cm^{-1} assigned to OH stretching and bending of physisorbed water molecules.[80] The IR bands observed at about 2925 cm^{-1}, 2852 cm^{-1} and 1384 cm^{-1} are attributed to asymmetric stretching, symmetric stretching and bending vibration of C–H bond, respectively.[81] The IR band at about 1178 cm^{-1} corresponds to C–N stretching.[82] The IR spectrum of SnS_2 nanoparticles shows an additional band at 862 cm^{-1} assigned to C–H bending.[83] The band at about 611 cm^{-1} is assigned to Sn–S stretching.[84]

3.3 Thermogravimetric analysis

The TGA curves of TiO_2–NaOH, SnS_2 nanoparticles, and TiO_2@SnS_2 core–shell nanocomposites are given in Fig. S6. The DTG plot for TiO_2–NaOH is given in Fig. S7. The TiO_2–NaOH microspheres show a two-step weight loss of about 3% in the temperature range of 30–1000 °C. The first weight loss of ∼1.3% below 350 °C is due to the loss of physisorbed water molecules.[85] The second weight loss of about 1.7% between 650 °C and 800 °C is due to the loss of chemically bonded OH groups from the surface of TiO_2 (dehydroxylation) and conversion of anatase TiO_2 to rutile phase.[68] The TGA curve of SnS_2 nanoparticles shows a three-step weight loss pattern. The first weight loss of about 3% below 230 °C is due to the loss of surface-adsorbed water molecules. The second weight loss of about 48.5% between 230 °C and 440 °C is attributed to the removal of organic moieties. The third weight loss of about 15.5% is due to oxidation of SnS_2 into SnO_2.[86] The TiO_2@SnS_2 core–shell nanocomposites (TiO_2–SnS_2-0.05, TiO_2–SnS_2-0.1 and TiO_2–SnS_2-0.15) show two-step weight loss patterns. The first weight loss of ∼3.0%, 3.1% and 3.8%, respectively, observed below 440 °C is due to the loss of physisorbed water molecules and removal of organic moieties. The second weight loss of about 1.9%, 3.4%, and 3.6%, respectively, between 440 °C and 530 °C is attributed to oxidation of SnS_2 into SnO_2.[87] The TGA studies indicate a total weight loss of about 4.9%, 6.5% and 7.4% in TiO_2–SnS_2-0.05, TiO_2–SnS_2-0.1, and TiO_2–SnS_2-0.15. In the core–shell nanocomposites, the % weight loss due to TiO_2 is negligible and it is primarily due to the presence of SnS_2 in the TiO_2@SnS_2 core–shell nanocomposites. In the TiO_2@SnS_2 core–shell nanocomposites, an increase in weight loss is observed with increase in the concentration of SnS_2 nanoparticles (shell) on the TiO_2 core.

3.4 FESEM and EDX analyses

The coating of SnS_2 nanoparticles over the TiO_2 microspheres was first done using unmodified as-prepared TiO_2 (*i.e.*, before calcination) and unmodified calcined TiO_2 microspheres. Fig. S8 shows the FESEM images of TiO_2@SnS_2 nanocomposites synthesized using unmodified as-prepared TiO_2 and unmodified calcined TiO_2 microspheres. The EDX results (Table S2) give distribution of different elements (Ti, O, Sn and S) in the thus prepared TiO_2@SnS_2 nanocomposites. Both FESEM and EDX results of TiO_2@SnS_2 nanocomposites, synthesized using as-prepared TiO_2 and unmodified calcined TiO_2 microspheres, indicate non-uniform coating of SnS_2 nanoparticles on the TiO_2 microspheres. Hence, the synthesis of TiO_2@SnS_2 core–shell nanocomposites was attempted using NaOH-modified TiO_2 microspheres. The SEM images of TiO_2–NaOH, SnS_2 nanoparticles, and TiO_2@SnS_2 core–shell nanocomposites, synthesized using TiO_2–NaOH microspheres as the core, are given in Fig. S9. The FESEM image of TiO_2–NaOH microspheres displays spherical particles with a diameter of about 471 ± 17 nm. The FESEM image of SnS_2 nanoparticles shows flake-like morphology. The FESEM images of TiO_2@SnS_2 core–shell nanocomposites (TiO_2–SnS_2-0.05, TiO_2–SnS_2-0.1 and TiO_2–SnS_2-0.15) show that SnS_2 nanoparticles are uniformly coated over the TiO_2–NaOH microspheres. The EDX results (Table S3) indicate uniform distribution of different elements (Ti, O, Sn, and S) in all the core–shell nanocomposites. In the TiO_2@SnS_2 core–shell nanocomposites, an increase in weight% of Sn and S is observed with an increase in $[Sn^{4+}]:[S^{2-}]$ ratio used during their synthesis.

3.5 TEM analysis

The TEM micrographs of TiO_2–NaOH, SnS_2 nanoparticles, and TiO_2@SnS_2 core–shell nanocomposites are displayed in Fig. 2. The TiO_2–NaOH microspheres show spherical morphology with a diameter of about 488 nm. The SnS_2 nanoparticles show flake-like morphology. The flake thickness was estimated using the TEM image. The particle size histogram is shown in Fig. S10, and the mean thickness is about 52 ± 12 nm. The TEM micrographs of TiO_2@SnS_2 core–shell nanocomposites (TiO_2–SnS_2-0.05, TiO_2–SnS_2-0.1 and TiO_2–SnS_2-0.15) show uniform coating of SnS_2 nanoparticles on the TiO_2 microspheres. Table 2 summarizes the particle diameter, core size and shell thickness observed from the TEM micrographs of TiO_2@SnS_2 core–shell nanocomposites. The overall diameter of TiO_2@SnS_2 core–shell nanocomposites varies from 457 nm to 503 nm. The core diameter in the TiO_2@SnS_2 core–shell nanocomposites varies from 434 nm to 489 nm. The thickness of the shell (SnS_2 nanoparticles) over the TiO_2 microspheres varies from 14 nm to 26 nm. This variation of thickness of the shell is due to the synthetic conditions. Use of different amounts of $SnCl_4 \cdot 5H_2O$ and thiourea during the synthesis of TiO_2@SnS_2 core–shell nanocomposites leads to variation in shell thickness. The EDS spectrum and elemental analysis data (from TEM measurements) for TiO_2–SnS_2-0.15 are given in Fig. S11 and Table S4, respectively. The TEM EDS analysis was performed at three different spots and the results confirm the uniform presence of Ti, Sn, S, and O in the core–shell nanocomposites (TiO_2–SnS_2-0.15). The EDS line scanning data and elemental mapping images (from SEM) of TiO_2@SnS_2 core–shell nanocomposites (TiO_2–SnS_2-0.15) are shown in Fig. 3. The EDS line scan (Fig. 3(a)) indicates that the concentration of titanium and oxygen at the edge is less and that of tin and sulfur is high. On moving from the edge to the centre of the particle, the concentration of Ti and O increases and that of Sn and S decreases. The elemental mapping results (Fig. 3(b)) also indicate that Sn and S are predominantly located at the edges of TiO_2 microspheres. On the other hand, Ti and O are present more at the centre. This indicates the successful formation of TiO_2@SnS_2 core–shell nanocomposites.

The SAED patterns of TiO_2–NaOH microspheres, SnS_2 nanoparticles, and TiO_2@SnS_2 core–shell nanocomposites are displayed in Fig. S12. The SAED pattern of TiO_2–NaOH microspheres shows rings that correspond to the planes of anatase

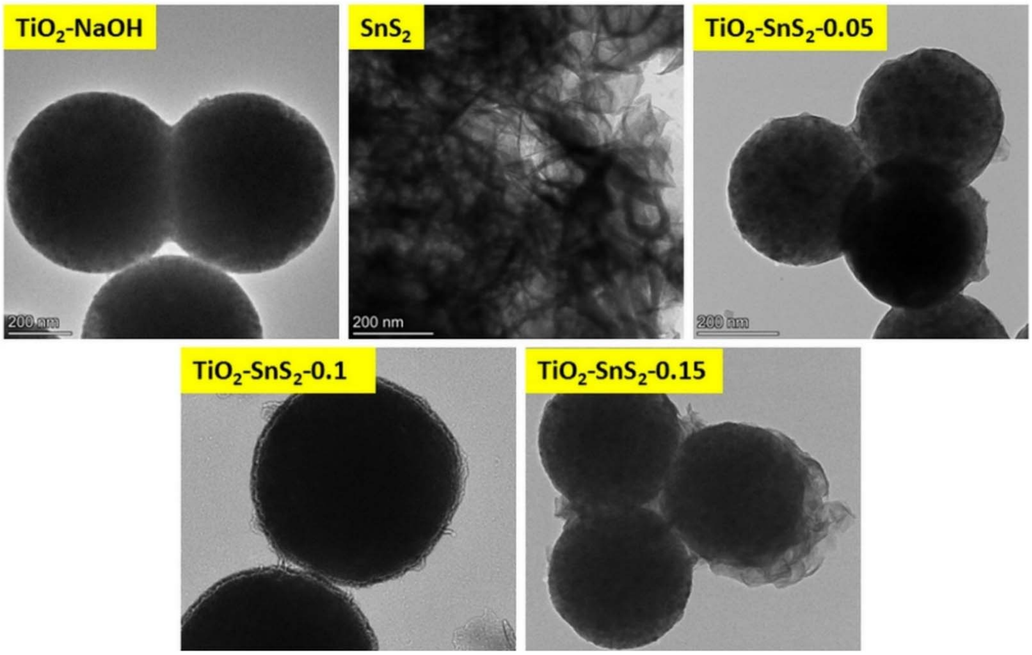

Fig. 2 TEM images of TiO_2–NaOH, SnS_2 nanoparticles and TiO_2@SnS_2 core–shell nanocomposites.

Table 2 Summary of results from TEM studies of TiO_2@SnS_2 core–shell nanocomposites

Sample code	Particle diameter (nm)	Flake thickness (nm)	Core size (nm)	Shell thickness (nm)
TiO_2–NaOH	488	—	—	—
SnS_2	—	52 ± 12	—	—
TiO_2–SnS_2-0.05	457	—	434	14
TiO_2–SnS_2-0.1	478	—	456	21
TiO_2–SnS_2-0.15	503	—	489	26

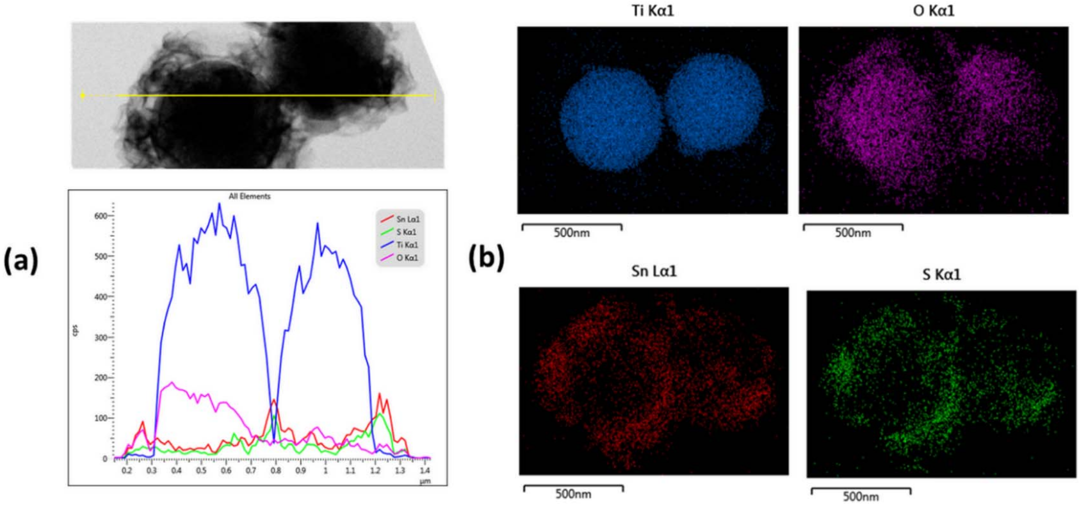

Fig. 3 (a) EDS line scan and (b) elemental mapping data of TiO_2–SnS_2-0.15 core–shell nanocomposite.

TiO_2 (JCPDS file no. 84-1286). The rings, observed in the SAED pattern of SnS_2 nanoparticles, correspond to the planes of SnS_2 (JCPDS file no. 83-1705). The SAED patterns of TiO_2@SnS_2 core–shell nanocomposites (TiO_2–SnS_2-0.05, TiO_2–SnS_2-0.1 and TiO_2–SnS_2-0.15) show rings attributed to reflections due to both TiO_2 and SnS_2.

The HRTEM images of TiO_2–NaOH microspheres, SnS_2 nanoparticles, and TiO_2@SnS_2 core–shell nanocomposites are given in Fig. S13. The observed lattice fringes in the HRTEM image of TiO_2–NaOH with a *d* spacing of 3.49 Å are attributed to the (101) plane of TiO_2 (JCPDS file no. 84-1286). The lattice fringes in the HRTEM image of SnS_2 nanoparticles with a *d* spacing of 3.15 Å is attributed to the (100) plane of SnS_2 (JCPDS file no. 83-1705). The *d* spacing values (estimated from the lattice fringes) of TiO_2@SnS_2 core–shell nanocomposites (TiO_2–SnS_2-0.05, TiO_2–SnS_2-0.1 and TiO_2–SnS_2-0.15) are 3.49 Å and 3.15 Å attributed to the (101) plane of TiO_2 and (100) plane of SnS_2, respectively. The specific surface area of TiO_2–NaOH microspheres, SnS_2 nanoparticles, and TiO_2@SnS_2 core–shell nanocomposites (TiO_2–SnS_2-0.05, TiO_2–SnS_2-0.1 and TiO_2–SnS_2-0.15), as measured by the BET method, are 9 $m^2\ g^{-1}$, 17 $m^2\ g^{-1}$, 10 $m^2\ g^{-1}$, 13 $m^2\ g^{-1}$, and 19 $m^2\ g^{-1}$, respectively.

3.6 Optical properties

The optical properties of TiO_2–NaOH microspheres, SnS_2 nanoparticles, and TiO_2@SnS_2 core–shell nanocomposites were studied using UV-Vis DRS spectroscopy (Fig. 4) and the Tauc plots (Fig. S14) were used to estimate the band gap. The UV-Vis DRS measurements were done three times for each sample. Table S5 includes error bars for the band gap.[88] The band gap of TiO_2–NaOH microspheres and SnS_2 nanoparticles are 3.1 eV and 2.03 eV, respectively. The TiO_2@SnS_2 core–shell nanocomposites (TiO_2–SnS_2-0.05, TiO_2–SnS_2-0.1 and TiO_2–SnS_2-0.15) have band gaps of 2.23 eV, 2.18 eV and 2.15 eV, respectively. The TiO_2@SnS_2 core–shell nanocomposites exhibit band gap only due to SnS_2 suggesting that the TiO_2 microspheres are coated with a thick shell of SnS_2 nanoparticles. The band gap values were also estimated using K–M plots[89] (Fig. S15) and the values are summarized in Table S5. Although the band gap of a semiconductor can be estimated using both Tauc plots and K–M plots, the band gap values estimated using K–M plots can often be misleading. This is because the K–M function is proportional to the ratio of the absorption and scattering coefficients (α) and is considered as an approximate. Furthermore, the K–M function does not consider the nature of the electronic transition (direct or indirect in a semiconductor).[90]

3.7 PL spectroscopy

The PL spectra of TiO_2@SnS_2 core–shell nanocomposites (λ_{exc} = 450 nm) are shown in Fig. 5. The PL spectra of TiO_2–NaOH microspheres, SnS_2 nanoparticles, and TiO_2@SnS_2 core–shell nanocomposites exhibit an emission peak at ~590 nm. This emission peak is due to the recombination of electrons with holes that are trapped above the valence state.[91–93] The emission peak at about 590 nm in SnS_2 nanoparticles is due to the near band edge emission of the SnS_2 phase.[94] The order of PL intensity in the samples is: TiO_2–NaOH > SnS_2 > TiO_2–SnS_2-0.05 > TiO_2–SnS_2-0.1 > TiO_2–SnS_2-0.15. The PL intensity is the least for TiO_2–SnS_2-0.15 and it is expected to show the highest photocatalytic activity among all the samples.

3.8 XPS analysis

The oxidation states of different elements present in TiO_2–NaOH microspheres, SnS_2 nanoparticles and TiO_2@SnS_2 core–shell nanocomposite (TiO_2–SnS_2-0.15) were determined by XPS analysis, and the results are given in Fig. 6. Table S6 summarizes binding energies of all the elements (Ti, O, Sn and S) present in the samples. As shown in the Ti 2p spectrum of TiO_2–NaOH (Fig. 6(a)), the peaks at 456.2 eV and 462.3 eV correspond to Ti $2p_{3/2}$ and Ti $2p_{1/2}$ of Ti^{4+}, respectively. The O 1s spectrum of TiO_2–NaOH shows peaks at 530.9 eV and 532.1 eV due to lattice oxygen (O^{2-}) and surface hydroxyl (OH) oxygen, respectively.[95,96] The Sn 3d spectrum of SnS_2 nanoparticles (Fig. 6(b)) shows peaks at 486.0 eV and 494.4 eV due to Sn $3d_{5/2}$ and Sn $3d_{3/2}$ of Sn^{4+}, respectively. The S 2p spectrum of SnS_2 nanoparticles shows peaks at 165.0 eV and 166.2 eV corresponding to S $2p_{3/2}$ and S $2p_{1/2}$, respectively.[97] The XPS spectrum of the TiO_2@SnS_2 core–shell nanocomposite (TiO_2–SnS_2-0.15) is shown in Fig. 6(c). The Ti 2p spectrum of TiO_2–SnS_2-0.15 shows peaks at 458.0 eV and 463.7 eV attributed to Ti $2p_{3/2}$ and Ti $2p_{1/2}$ of Ti^{4+}, respectively. The O 1s spectrum of TiO_2–SnS_2-0.15 shows peaks at 531.0 eV and 532.3 eV assigned to lattice oxygen and surface hydroxyl oxygen, respectively.[95,96] The Sn 3d spectrum of TiO_2–

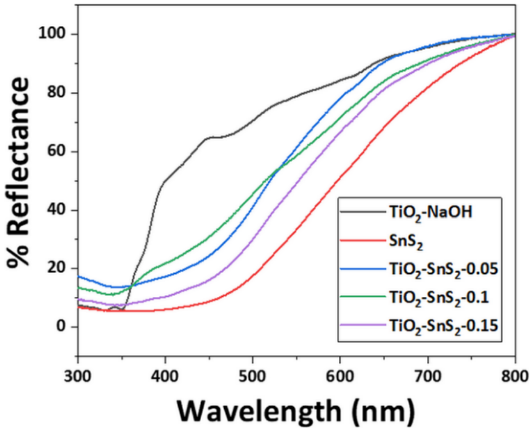

Fig. 4 UV-Vis DRS spectra of TiO_2–NaOH, SnS_2 nanoparticles and TiO_2@SnS_2 core–shell nanocomposites.

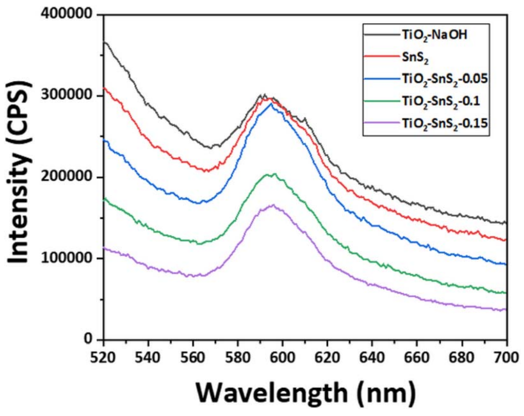

Fig. 5 PL spectra of TiO_2–NaOH, SnS_2 nanoparticles and TiO_2@SnS_2 core–shell nanocomposites.

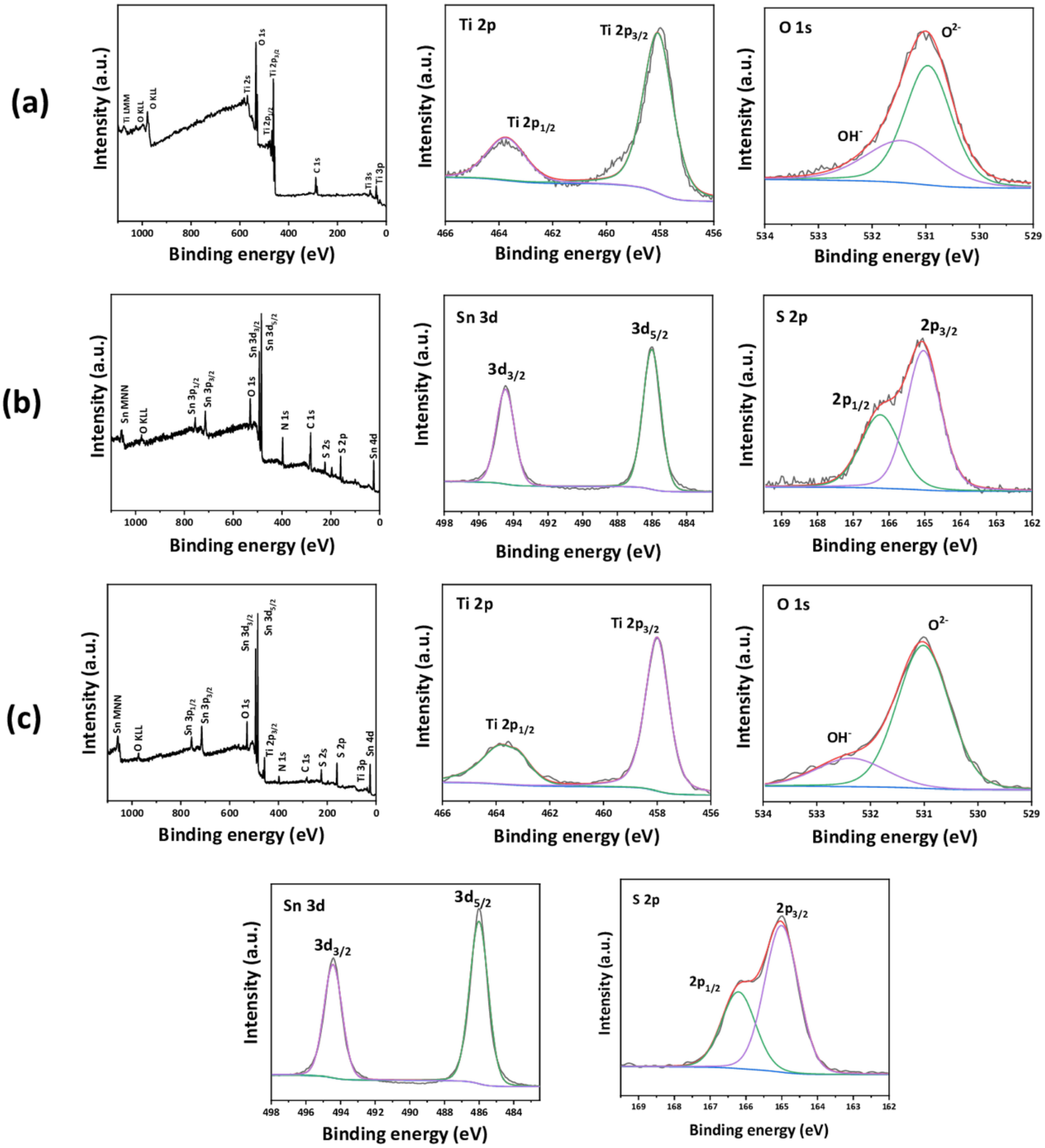

Fig. 6 XPS spectra of (a) TiO_2–NaOH microspheres, (b) SnS_2 nanoparticles and (c) TiO_2@SnS_2 core–shell nanocomposite (TiO_2–SnS_2-0.15).

SnS_2-0.15 shows peaks at 485.9 eV and 494.3 eV due to Sn $3d_{5/2}$ and Sn $3d_{3/2}$ of Sn^{4+}, respectively. The S 2p spectrum of TiO_2–SnS_2-0.15 shows peaks at 164.9 eV and 166.2 eV due to S $2p_{3/2}$ and S $2p_{1/2}$, respectively.[97]

There is a minor decrease in Sn 3d and S 2p binding energy values on going from pure SnS_2 nanoparticles to the TiO_2@SnS_2 core–shell nanocomposites. Also, a minor increase in Ti 2p and O 1s binding energies is observed on going from pure TiO_2 microspheres (TiO_2–NaOH) to the core–shell nanocomposites. The shifts in binding energies in the XPS spectrum of the TiO_2@SnS_2 core–shell nanocomposite could be due to electron transfer from the core (TiO_2) to the shell (SnS_2) during the formation of the core–shell nanocomposite. The electron transfer leads to a partial positive charge on TiO_2, leading to an increase in binding energies of Ti 2p and O 1s and a partial negative charge on SnS_2, leading to a decrease in binding energies of Sn 3d and S 2p.[98–100]

To investigate the charge transfer and band (VB and CB) positions in TiO_2@SnS_2 core–shell nanocomposites, XPS-VB (UPS spectra) measurements were performed. Fig. S16 provides the XPS-VB spectra of TiO_2–NaOH microspheres, SnS_2 nanoparticles and TiO_2–SnS_2-0.15. The valence band positions estimated from the XPS-VB spectra for TiO_2–NaOH microspheres, SnS_2 nanoparticles and TiO_2–SnS_2-0.15 are 2.83 eV, 1.35 eV and 1.78 eV, respectively. In the TiO_2@SnS_2 core–shell nanocomposites, electron transfer occurs from the core (TiO_2) to the shell (SnS_2). The intermediate valence band position of TiO_2–SnS_2-0.15 suggests successful heterostructure formation and interfacial charge transfer between TiO_2 and SnS_2.[101,102] From the optical studies (DRS spectra), the band gaps for TiO_2–NaOH and SnS_2 are 3.1 eV and 2.02 eV, respectively. On applying the equation, $E_{CB} = E_{VB} - E_g$, the conduction band positions of TiO_2–NaOH and SnS_2 nanoparticles are −0.27 eV and −0.67 eV, respectively. To further confirm the charge transfer in TiO_2@-SnS_2 core–shell nanocomposites, EIS measurements were also performed (see Section 3.15 for more details).

3.9 Mechanism of formation of TiO_2@SnS_2 core–shell nanocomposites

Scheme 1 illustrates the proposed mechanism of formation of TiO_2@SnS_2 core–shell nanocomposites. At first, on surface modification with NaOH, hydroxyl groups are attached on the surface of TiO_2 microspheres. This can be evidenced from the IR spectral studies (Fig. S4). Due to the presence of hydroxyl groups on the surface of TiO_2 microspheres, Sn^{4+} ions are attached on the surface of TiO_2 *via* electrostatic interaction. This is followed by the thermal decomposition of thiourea to form H_2S and the formation of TiO_2@SnS_2 core–shell nanocomposites. The reactions involved in the formation of SnS_2 nanoparticles over TiO_2–NaOH microspheres are given in eqn (3) and (4).[103–105]

$$SC(NH_2)_2 \xrightarrow{150^\circ C} NH_2CN + H_2S \tag{3}$$

$$Sn^{4+} + S^{2-} \rightarrow SnS_2 \tag{4}$$

SnS_2 nanoflakes are formed by the thermal decomposition of $SnCl_4 \cdot 5H_2O$ and thiourea in DPE. The formation of nanoflakes is a two-step process, *i.e.*, nucleation followed by growth.[106] At first, tin chloride reacts with thiourea leading to the formation of a small cluster of SnS_2 (nuclei). The presence of chloride ions leads to oriented growth of particles. The chloride ions adsorbed on the transverse planes of SnS_2 particles inhibit growth in those directions. As a result, the growth occurs in the longitudinal axis leading to the formation of SnS_2 nanoflakes.[82]

3.10 Photocatalytic activity

The photocatalytic activity of TiO_2@SnS_2 core–shell nanocomposites was studied using crystal violet as the dye pollutant (see Section 2.3 for more details). As indicated by the UV-Vis spectral results (Fig. 7) on the photodegradation experiments, TiO_2–SnS_2-0.15 achieved about 99% degradation of crystal violet within 60 minutes under sunlight. TiO_2–NaOH microspheres, SnS_2 nanoparticles, TiO_2–SnS_2-0.05, and TiO_2–SnS_2-0.1 degrade about 53.1%, 60.2%, 61.5%, and 78.2% of crystal violet, respectively. This indicates that TiO_2–SnS_2-0.15 is a better photocatalyst for the degradation of crystal violet compared to

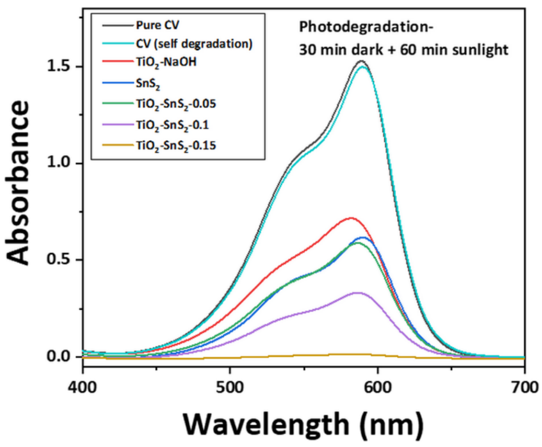

Fig. 7 UV-Vis spectral results indicating the photodegradation of CV using TiO_2@SnS_2 core–shell nanocomposites.

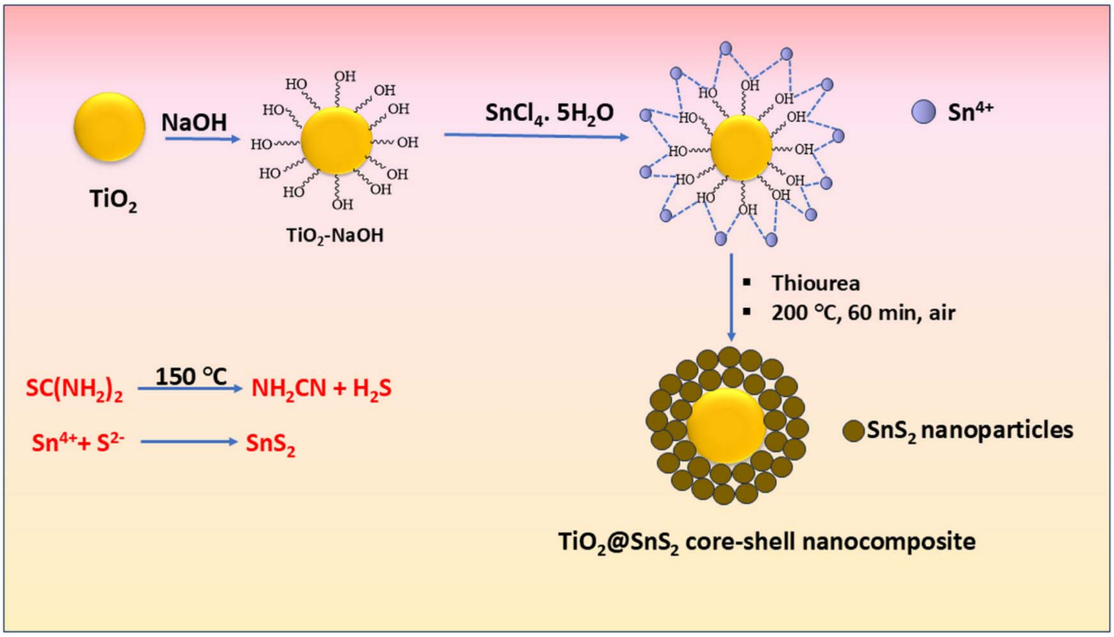

Scheme 1 Mechanism of formation of TiO_2@SnS_2 core–shell nanocomposites.

TiO_2–NaOH microspheres, SnS_2 nanoparticles and other core–shell nanocomposites. The self-degradation of crystal violet under sunlight, tested in the absence of any catalyst, was about 1.9%.

Furthermore, dark experiments were carried out in the absence of sunlight to understand adsorption of CV on the $TiO_2@SnS_2$ core–shell nanocomposites. In this experiment, 5 mg of each catalyst was taken in a test tube to which 5 mL of CV aqueous solution (2×10^{-5} M) was added. The test tubes were sonicated for one min followed by keeping them in the dark for 30 min/90 min. The UV-Vis absorbance spectra recorded for the supernatant solutions obtained after centrifugation of each mixture are shown in Fig. S17. The % adsorption by TiO_2–NaOH microspheres, SnS_2 nanoparticles and $TiO_2@SnS_2$ core–shell nanocomposites (TiO_2–SnS_2-0.05, TiO_2–SnS_2-0.1 and TiO_2–SnS_2-0.15) are 15%, 28.1%, 31.3%, 37.9% and 49%, respectively in 30 min and 26%, 47.9%, 34.8%, 39.9% and 53.8%, respectively in 90 min. The adsorption and photodegradation studies indicate that the $TiO_2@SnS_2$ core–shell nanocomposites act as a good photocatalyst for the degradation of CV and not as an adsorbent.

Furthermore, kinetic experiments were carried out by taking 6 test tubes each containing 5 mg of catalyst (TiO_2–NaOH microspheres, SnS_2 nanoparticles, and $TiO_2@SnS_2$ core–shell nanocomposites (TiO_2–SnS_2-0.05, TiO_2–SnS_2-0.1 and TiO_2–SnS_2-0.15)) and 5 mL of CV aqueous solution (2×10^{-5} M). The mixtures were kept in the dark for 30 min which was followed by irradiation with sunlight for different time periods (10–60 min). UV-Vis spectra were recorded for the supernatant solutions obtained after centrifuging the mixture in each test tube.

The kinetics results are shown in Fig. 8(a) and TiO_2–SnS_2-0.15 shows maximum degradation in 60 min. The kinetics of photodegradation of CV by TiO_2–SnS_2-0.15 follows pseudo 1st order kinetics as indicated by $-\ln(C_t/C_0)$ against irradiation time plots shown in Fig. 8(b). The rate constant values were determined using the kinetic curves. Table 3 summarizes the % adsorption (30 min/90 min), % total degradation (90 min), % photodegradation only, rate constant and R^2 values for TiO_2–NaOH microspheres, SnS_2 nanoparticles and $TiO_2@SnS_2$ core–shell nanocomposites (TiO_2–SnS_2-0.05, TiO_2–SnS_2-0.1 and TiO_2–SnS_2-0.15). The rate constant values are in the order: TiO_2–SnS_2-0.15 > TiO_2–SnS_2-0.1 > TiO_2–SnS_2-0.05 > SnS_2 > TiO_2–NaOH indicating that TiO_2–SnS_2-0.15 is the best photocatalyst among all the samples. The better photocatalytic activity of TiO_2–SnS_2-0.15 is attributed to a lower rate of recombination of electron and hole pairs in TiO_2–SnS_2-0.15 as indicated by the PL spectral studies (Fig. 5). The photocatalytic degradation results were compared with those reported in the literature (Table S7).[24,107–128] In the literature, more time (70–390 min) is required for the photodegradation of CV. Wherever lesser time is reported (30–45 min),[116,117] either the amount of catalyst used is high (250 mg/100 mL) or the % photodegradation is less (83–93%). The $TiO_2@SnS_2$ core–shell nanocomposites (*e.g.*, TiO_2–SnS_2-0.15), reported in the current work, achieved 99% degradation of CV within 60 minutes under sunlight.

3.11 Effect of pH

The photocatalytic degradation efficiency of a catalyst is affected by the pH of the solution. The effect of pH on the photodegradation efficiency of TiO_2–SnS_2-0.15 was studied by varying the pH of the solution between 2 and 10. The pH of the solutions was varied using 0.1 M HCl and 0.1 M NaOH. The experiment was performed by taking 5 mg of catalyst (TiO_2–SnS_2-0.15) in 5 mL of CV aqueous solution (2×10^{-5} M) at different pH values (2–10) in different test tubes. The contents were kept in the dark (for 30 min) followed by irradiation with sunlight for 60 min and UV-Vis absorbance spectra were measured for the supernatant solutions obtained after centrifugation. The variation of the photodegradation efficiency of TiO_2–SnS_2-0.15 with pH is shown in Fig. S18(a). The results indicate that maximum photocatalytic efficiency is observed at pH = 7.

At lower pH, there are more H^+ ions in the solution that make the surface of the catalyst positively charged (zeta potential = + 19.0 mV at pH = 4). Crystal violet is a cationic dye, and it will experience electrostatic repulsion towards the surface

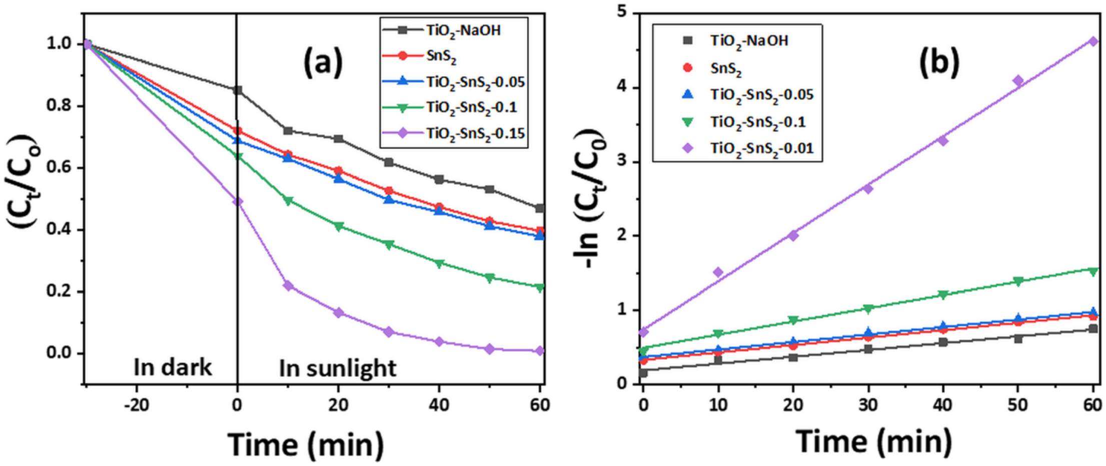

Fig. 8 (a) (C_t/C_0) plots and (b) $-\ln(C_t/C_0)$ *vs.* time plots for TiO_2–NaOH microspheres, SnS_2 nanoparticles and $TiO_2@SnS_2$ core–shell nanocomposites as the catalyst for the photodegradation of CV.

Table 3 Photocatalytic degradation results of crystal violet using $TiO_2@SnS_2$ core–shell nanocomposites

Sample code	% Adsorption (30 min)	% Adsorption (90 min)	Total degradation% (30 min dark + 60 min sunlight)	Photodegradation % only (60 min)	Rate constant for photodegradation (min^{-1})	R^2
TiO_2–NaOH	15.0	26.0	53.1	38.1	9.1×10^{-3}	0.98
SnS_2	28.1	47.9	60.2	32.1	9.5×10^{-3}	0.98
TiO_2–SnS_2-0.05	31.3	34.8	61.5	30.2	1.0×10^{-2}	0.99
TiO_2–SnS_2-0.1	37.9	39.9	78.2	38.3	1.7×10^{-2}	0.99
TiO_2–SnS_2-0.15	49.0	53.8	99.0	50.0	6.4×10^{-2}	0.99

of the catalyst in an acidic medium leading to a decrease in the photocatalytic efficiency. On the other hand, in basic medium, the presence of more OH^- ions in the solution will lead to a negatively charged catalyst surface (zeta potential = −21.4 mV at pH = 10). This results in an electrostatic attraction towards crystal violet leading to higher photodegradation efficiency by the catalyst.[129]

3.12 Effect of catalyst dosage

To determine the optimum amount of catalyst required to degrade CV using $TiO_2@SnS_2$ core–shell nanocomposites, the effect of catalyst dosage on the photodegradation efficiency was studied. The catalyst (TiO_2–SnS_2-0.15) was taken in different amounts (1–8 mg) in 5 mL of aqueous CV solution (2×10^{-5} M) in test tubes. The mixtures were kept in the dark (for 30 min) followed by sunlight irradiation for 60 min and the UV-Vis absorbance spectra were measured for the supernatant solutions obtained after centrifugation. The UV-Vis spectral results shown in Fig. S18(b) indicate that 5 mg of TiO_2–SnS_2-0.15 in 5 mL of CV is the optimum catalyst dosage for the photodegradation of CV.[130]

3.13 Scavenger tests

To understand the mechanism of photodegradation of CV by TiO_2–SnS_2-0.15, scavenger tests were performed. Different scavengers (isopropyl alcohol (IPA), ammonium oxalate (AO) and *p*-benzoquinone (PBQ)) were used to trap $OH^•$, $O_2^{•-}$ and h^+, respectively.[127,131] In a typical experiment, 10 mM of scavenger was added to 5 mL aqueous solution of CV (2×10^{-5} M) followed by the addition of 5 mg of catalyst (TiO_2–SnS_2-0.15). The contents were kept in the dark (for 30 min) followed by irradiation with sunlight for 60 min and UV-Vis absorbance spectra were measured for the supernatant solutions obtained after centrifugation. The scavenger test results (Fig. S19) show a decrease of about 15.2%, 39.4% and 53.4% in the presence of IPA, PBQ, and AO, respectively. This indicates that $O_2^{•-}$ and h^+ are the major species responsible for the photodegradation of CV using $TiO_2@SnS_2$ core–shell nanocomposites as the catalyst.

3.14 Mechanism of photodegradation of crystal violet

Crystal violet degrades *via* two different pathways, *i.e.*, *N*-demethylation and oxidative degradation.[106,132] In the first case, reactive oxygen species (ROS) attack the *N*,*N*-dimethyl groups of the CV molecules leading to the formation of *N*-de-methylated CV species. In the second case, the ROS species attack the central carbon of CV facilitated by its conjugated aminotriphenylmethane structure leading to disruption in the conjugation and decolourisation of CV. This step leads to the formation of intermediates such as 4-(*N*,*N*-dimethylamino)-4′-(*N*′,*N*′-dimethylamino)benzophenone and 4-(*N*,*N*-dimethylamino)phenol. Both these steps can occur simultaneously or one-by-one.[132] The formed intermediates undergo further oxidation leading to ring opening and complete mineralisation of CV leading to formation of CO_2 and H_2O.[133]

Scheme 2 gives the proposed mechanism of photodegradation of crystal violet in the presence of $TiO_2@SnS_2$ core–shell nanocomposites as the catalyst. The valence band (VB) and conduction band (CB) positions of TiO_2 are located at 2.83 eV and −0.27 eV, respectively.[134] The VB and CB of SnS_2 are located at 1.35 eV and −0.67 eV, respectively,[46] indicating a more negative band potential than that of TiO_2 (see Section 3.8, XPS-VB results).

Upon irradiation with sunlight, electrons in the VB of SnS_2 are excited to its CB, leaving behind photogenerated holes. Due to the favourable band alignment, the excited electrons in the CB of SnS_2 migrate to the CB of TiO_2, while the holes in the VB of TiO_2 migrate to that of SnS_2. This charge transfer effectively suppresses electron–hole recombination, enhancing the photocatalytic activity. The electrons in the CB of TiO_2 interact with dissolved O_2 molecules to generate superoxide radicals ($O_2^{•-}$), while the holes in the VB of SnS_2 oxidize water molecules to produce $OH^•$. These highly reactive species then attack and degrade crystal violet molecules into harmless end products (CO_2 and H_2O).[129,135,136]

The standard potential for $O_2/O_2^{•-}$ is −0.33 V and that for $OH^-/OH^•$ is 2.38 V. The VB of TiO_2 (2.83 V) is more positive than that of $OH^-/OH^•$ (2.38 V) indicating that $OH^•$ could be generated. Similarly, the conduction band of SnS_2 (−0.67 V) is more negative than that of $O_2/O_2^{•-}$ (−0.33 V) indicating that $O_2^{•-}$ could also be generated. The generation of both $OH^•$ and $O_2^{•-}$ by $TiO_2@SnS_2$ core–shell nanocomposites on solar irradiation leads to the degradation of crystal violet into CO_2 and H_2O as shown in Scheme 2.

3.15 EIS studies

Electrochemical Impedance Spectroscopy (EIS) measurements were performed for TiO_2–NaOH, SnS_2 nanoparticles and $TiO_2@SnS_2$ core–shell nanocomposites (TiO_2–SnS_2-0.05, TiO_2–SnS_2-0.1 and TiO_2–SnS_2-0.15) to understand the charge separation. The samples were deposited onto FTO (fluorine-doped tin oxide) glass substrates (dimensions: 1 cm × 2 cm). For each

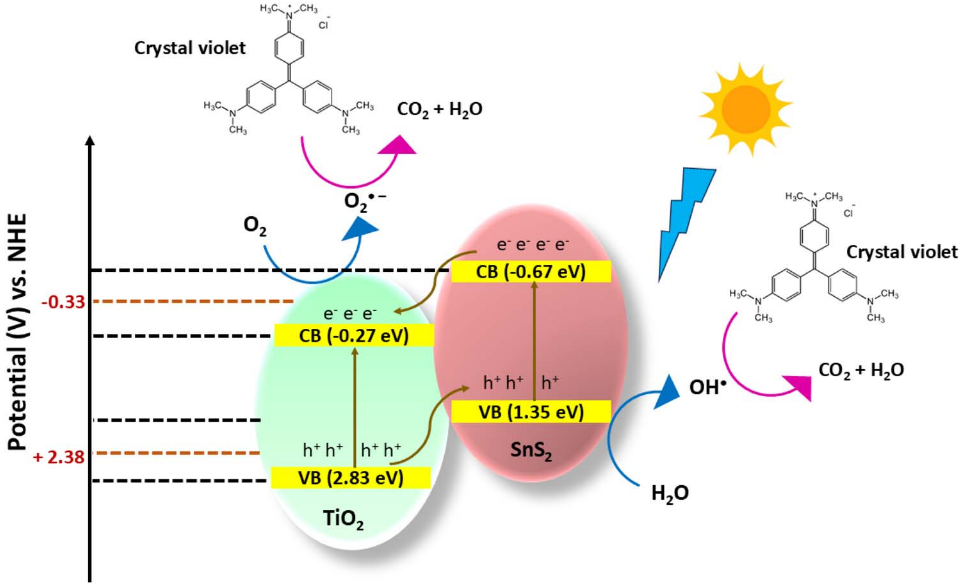

Scheme 2 Mechanism of photodegradation of crystal violet using TiO_2@SnS_2 core–shell nanocomposites as the catalyst.

sample, 30 mg of the sample (TiO_2–NaOH, SnS_2 nanoparticles and TiO_2@SnS_2 core–shell nanocomposites) was dispersed in 3 mL of ethanol to form a homogeneous slurry. The mixture was subjected to sonication for 45 minutes to ensure uniform dispersion. Subsequently, the slurry was drop-cast onto the FTO substrates and dried in an oven (at ~50 °C).

The electrochemical measurements were conducted using a conventional three-electrode system. The modified FTO glass slides (coated with TiO_2–NaOH, SnS_2 and TiO_2@SnS_2 core–shell nanocomposites) served as the working electrode. Ag/AgCl electrode was employed as the reference electrode. A platinum wire was employed as the counter electrode. The EIS measurements were performed in 0.1 M KOH aqueous solution as the electrolyte, over a frequency range of 0.1 Hz to 100 kHz (Multi Autolab/M204 electrochemical workstation (Metrohm Autolab B·V., Netherlands)).

Fig. S20 provides the Nyquist plots for all the samples. The order of arc radius is as follows: TiO_2–NaOH > SnS_2 > TiO_2–SnS_2-0.05 > TiO_2–SnS_2-0.1 > TiO_2–SnS_2-0.15. The arc radius in the Nyquist plot corresponds to charge transfer resistance (R_{ct}) at the interface of the electrode and electrolyte.[137] A smaller arc radius indicates lower charge-transfer resistance (R_{ct}), which suggests faster interfacial charge transfer. The smaller arc radius observed in TiO_2–SnS_2-0.15 among all the samples suggests faster interfacial charge transfer and thus its better photocatalytic efficiency towards degradation of crystal violet compared to the other samples.

3.16 Time resolved PL decay experiments

PL decay experiments were performed using an FLS-1000-xs-t (Edinburgh Instruments) system for TiO_2–NaOH microspheres, SnS_2 nanoparticles, and TiO_2@SnS_2 core–shell nanocomposites (TiO_2–SnS_2-0.05, TiO_2–SnS_2-0.1 and TiO_2–SnS_2-0.15) and the data are presented in Fig. S21. The excitation and emission wavelengths were 450 nm and 590 nm, respectively. The PL decay curves were well fitted according to the bi-exponential function in the form of $R(t) = A + B_1 \exp(-t/\tau_1) + B_2 \exp(-t/\tau_2)$.

Where, A is a constant background offset, B_1 and B_2 are amplitude coefficients of the two decay components, τ_1 is the lifetime of the faster decay component and τ_2 is the lifetime of the slower decay component.

The average lifetime τ_{avg} was calculated using the formula $\tau_{avg} = (B_1\tau_1^2 + B_2\tau_2^2)/(B_1\tau_1 + B_2\tau_2)$.[138] Table S8 summarizes the fluorescence decay components for all the samples. The average lifetime (τ_{avg}) values estimated for TiO_2–NaOH microspheres, SnS_2 nanoparticles, TiO_2–SnS_2-0.05, TiO_2–SnS_2-0.1, and TiO_2–SnS_2-0.15 are 8.37 ns, 10.82 ns, 10.91 ns, 12.44 ns, and 14.39 ns, respectively. The observed trend in lifetime follows the order: TiO_2–SnS_2-0.15 > TiO_2–SnS_2-0.1 > TiO_2–SnS_2-0.05 > SnS_2 >TiO_2. TiO_2–SnS_2-0.15 exhibits a higher average PL decay lifetime indicating a slower recombination rate of photogenerated excitons, indicating more effective charge separation and better photocatalytic efficiency towards the degradation of crystal violet.

3.17 Detection of hydroxyl radicals

To prove the formation of hydroxyl radicals during the photodegradation of CV by TiO_2–SnS_2-0.15, PL spectral studies were performed using terephthalic acid. Terephthalic acid is non-fluorescent but on reaction with hydroxyl radicals, it produces 2-hydroxyl terephthalic acid, which is fluorescent.[139] About 40 mg of catalyst (TiO_2–SnS_2-0.15) was taken in a beaker containing an aqueous solution of terephthalic acid (5×10^{-4} M) and NaOH (2×10^{-3} M). After sunlight irradiation, PL spectra were recorded at periodic time intervals for the supernatant solutions obtained after centrifugation (λ_{exc} = 315 nm). An emission band at 425 nm (Fig. S22) is observed with an increase in PL intensity as a function of time indicating the generation of hydroxyl radicals with time.

3.18 Recyclability and scalability

Photodegradation experiments were performed repeatedly to understand the stability and reusability of TiO_2@SnS_2 core–shell nanocomposites. In this experiment, an aqueous solution containing 70 mg of catalyst (TiO_2–SnS_2-0.15) and 70 mL of CV aqueous solution (2×10^{-5} M) was kept in the dark (for 30 min) followed by irradiation with sunlight for 60 min. The UV-Vis absorbance spectrum was measured for the supernatant solution obtained after centrifugation. The catalyst was recovered by centrifugation and washed with methanol several times and finally dried in an oven at 60 °C for 12 h. Five cycles of photocatalytic degradation experiments were carried out using the catalyst recovered after each cycle. The recyclability test results (Fig. S23) show a decrease of about 12.5% in photodegradation efficiency of TiO_2–SnS_2-0.15 after 5 cycles indicating that TiO_2–SnS_2-0.15 is a photocatalyst with good recyclability. Furthermore, to determine the stability of the catalyst (TiO_2–SnS_2-0.15), characterization of the recovered catalyst was performed. Fig. S24 provides the XRD pattern, FT-IR spectrum and FESEM image of the catalyst recovered after the recyclability test. The post-recyclability EDX analysis results are provided in Table S9. The results indicate no change in the phase or morphology of the catalyst after repeated use indicating its high stability.

Nanomaterials have been explored as catalysts for photodegradation of toxic dyes by easy design using different synthetic approaches. Their size, chemical composition and morphology can be easily controlled using optimized synthetic conditions but due to various environmental concerns and economic viability, their large-scale use for environmental remediation is still limited. In the current work, TiO_2@SnS_2 core–shell nanocomposites demonstrate promising photocatalytic activity under laboratory conditions. The synthetic method and photodegradation results in the current study are reproducible, but large-scale production and long-term stability are unexplored.[140]

3.19 Potential application of TiO_2@SnS_2 core–shell nanocomposites as C-2 catalysts

Chemical reactions in which two carbon containing products (*e.g.*, ethanol, ethylene or acetic acid) are formed through C–C coupling reactions are called C-2 reactions. This is particularly relevant for electrocatalytic and photocatalytic CO_2 reduction and syngas conversion. For a material to be used as a catalyst in a C-2 reaction, the following properties are important: (a) the presence of active sites that can stabilise key intermediates such as *CO, $*CH_2$ and *CHO, (b) efficient separation of charge carriers (in photocatalysis), and (c) a favourable and stable surface that can promote C–C coupling under the reaction conditions.

Metal sulfide nanoparticles and their nanocomposites have been employed as catalysts for C-2 reactions. For example, $ZnIn_2S_4$ nanosheets activated by nitrogen-doped carbon have been used for electrocatalytic CO_2 reduction to ethanol.[141] SnO_2/SnS_2/Cu_2SnS_3 heterojunction has been used for photocatalytic reduction of CO_2 to ethanol.[142] The TiO_2@SnS_2 core–shell nanocomposites are potential materials as catalysts for C-2 reactions. They can catalyze C–C coupling reactions in the following ways. The formation of TiO_2@SnS_2 core–shell nanocomposites builds a type-II heterojunction between TiO_2 and SnS_2. On solar irradiation, SnS_2 absorbs photons and generates an electron–hole pair (see Section 3.14), reducing the recombination of photogenerated excitons and promoting long-lived charge carriers for surface reactions. In the second step, the photogenerated electrons in the CB of TiO_2 can be used for the formation of intermediate species such as *CO, *CHO or $*CH_3$ from CO_2/CO. SnS_2 is well known to stabilize intermediates such as *CO. Furthermore, the C–C coupling can occur in the third step *via* reductive dimerization of surface-bound *CO or $*CH_3$ on the catalyst's surface. This leads to the formation of C-2 species such as acetaldehyde. In the final step, the photogenerated electrons and protons (typically from water oxidation) can hydrogenate acetaldehyde to produce ethanol.

From XPS results (Section 3.8), it was found that charge transfer takes place from core TiO_2 to shell SnS_2, indicating interfacial charge redistribution.[46] An increase in binding energy is observed for Ti 2p and O 1s, whereas a decrease in binding energy is observed for Sn 3d and S 2p in the TiO_2@SnS_2 core–shell nanocomposites. This suggests that there is more electron density on the surface of SnS_2 after the formation of TiO_2@SnS_2 core–shell nanocomposites. The electron-rich SnS_2 surface is beneficial in stabilizing electrophilic species (C-1) such as CHO and provides them sufficient residence time for C–C coupling reactions and can enhance catalytic activity compared to the individual components.

4 Conclusions

In the present study, TiO_2@SnS_2 core–shell nanocomposites were synthesized using the thermal decomposition method using different $[Sn^{4+}]:[S^{2-}]$ ratios. The core–shell nanocomposites were characterized using several analytical techniques. The XRD results confirmed the presence of both TiO_2 and SnS_2 phases in the core–shell nanocomposites. FESEM and TEM analyses confirmed uniform coating of SnS_2 nanoparticles on the TiO_2 microspheres indicating their core–shell structure. The TiO_2@SnS_2 core–shell nanocomposites demonstrate good catalytic activity towards the photodegradation of CV in aqueous solutions under sunlight. The photocatalytic efficiency of TiO_2@SnS_2 core–shell nanocomposites is better than that of the individual constituents and other metal-sulfide based nanocomposites that are reported in the literature. The TiO_2@SnS_2 core–shell nanocomposites, reported in the present study, have other potential applications, *e.g.*, sodium-ion batteries, gas sensors, water splitting, *etc.*

Author contributions

Nainy Khera: Methodology, data collection and interpretation, writing – original draft. Pethaiyan Jeevanandam: Conceptualization, project administrat

Conflicts of interest

There are no conflicts to declare.

Data availability

All the data supporting this study have been included in the main manuscript and the SI.

Some additional data supporting this article have been included as part of SI. See DOI: https://doi.org/10.1039/d5na00533g.

Acknowledgements

Nainy Khera acknowledges Council of Scientific and Industrial Research (CSIR), Govt of India for the award of a fellowship (JRF/SRF). The authors express gratitude to Institute Instrumentation Centre (IIT Roorkee) for helping with necessary instrumental facilities. Thanks are due to the Department of Metallurgical and Materials Engineering, IIT Roorkee for providing the HRTEM facility.

References

1 Z. Kılıç, *Int. J. Hydrol.*, 2020, **4**, 239–241.
2 A. Rafiq, M. Ikram, S. Ali, F. Niaz, M. Khan, Q. Khan and M. Maqbool, *J. Ind. Eng. Chem.*, 2021, **97**, 111–128.
3 R. Al-Tohamy, S. S. Ali, F. Li, K. M. Okasha, Y. A. G. Mahmoud, T. Elsamahy, H. Jiao, Y. Fu and J. Sun, *Ecotoxicol. Environ. Saf.*, 2022, **231**, 113160.
4 Z. Zheng, J. He, Z. Zhang, A. Kumar, M. Khan, C. W. Lung and I. M. C. Lo, *Environ. Sci. Nano*, 2024, **11**, 1784–1816.
5 C. C. Chen, C. S. Lu, Y. C. Chung and J. L. Jan, *J. Hazard. Mater.*, 2007, **141**, 520–528.
6 Y. Zhang, X. Yu, H. Liu, X. Lian, B. Shang, Y. Zhan, T. Fan, Z. Chen and X. Yi, *Environ. Sci. Nano*, 2021, **8**, 2049–2058.
7 Y. Zhang, Z. Zhang, Y. Zhang, Y. Li and Y. Yuan, *J. Colloid Interface Sci.*, 2023, **651**, 117–127.
8 X. Yin, L. Liu and F. Ai, *Front. Chem.*, 2021, **9**, 1–9.
9 Y. Wan, J. Chen, J. Zhan and Y. Ma, *J. Environ. Chem. Eng.*, 2018, **6**, 6079–6087.
10 W. Xu, S. Zhu, Y. Liang, Z. Li, Z. Cui, X. Yang and A. Inoue, *Sci. Rep.*, 2015, **5**, 18125.
11 B. Sheng, J. Liu, Z. Li, M. Wang, K. Zhu, J. Qiu and J. Wang, *Mater. Lett.*, 2015, **144**, 153–156.
12 M. Baláž, E. Dutková, Z. Bujňáková, E. Tóthová, N. G. Kostova, Y. Karakirova, J. Briančin and M. Kaňuchová, *J. Alloys Compd.*, 2018, **746**, 576–582.
13 R. R. Srivastava, P. Kumar Vishwakarma, U. Yadav, S. Rai, S. Umrao, R. Giri, P. S. Saxena and A. Srivastava, *Front. Nanotechnol.*, 2021, **3**, 1–13.
14 D. Hong, W. Zang, X. Guo, Y. Fu, H. He, J. Sun, L. Xing, B. Liu and X. Xue, *ACS Appl. Mater. Interfaces*, 2016, **8**, 21302–21314.
15 A. Sadollahkhani, O. Nur, M. Willander, I. Kazeminezhad, V. Khranovskyy, M. O. Eriksson, R. Yakimova and P. O. Holtz, *Ceram. Int.*, 2015, **41**, 7174–7184.
16 H. D. Abdul kader, I. Sh. Mohammed and S. H. Ammar, *Environ. Nanotechnol. Monit. Manag.*, 2022, **17**, 100664.
17 J. Chen, Y. Liao, X. Wan, S. Tie, B. Zhang, S. Lan and X. Gao, *J. Solid State Chem.*, 2020, **291**, 121652.
18 X. Dong, J. Deng, M. Ge, S. Lu and Q. Zhu, *Chem. Phys. Lett.*, 2023, **833**, 140950.
19 M. F. Mubarak, H. Selim and R. Elshypany, *J. Environ. Health Sci. Eng.*, 2022, **20**, 265–280.
20 A. Habtamu and M. Ujihara, *RSC Adv.*, 2023, **13**, 12926–12940.
21 Q. Gao, J. Li, B. Liu and C. Liu, *J. Alloys Compd.*, 2023, **931**, 167430.
22 T. T. Salunkhe, V. Kumar, A. N. Kadam, M. Mali and M. Misra, *Ceram. Int.*, 2024, **50**, 1826–1835.
23 X. Zhang, X. Jia, R. Xu, X. Lu, H. Liu and Y. Niu, *J. Alloys Compd.*, 2022, **923**, 166315.
24 V. Gadore, S. R. Mishra and M. Ahmaruzzaman, *J. Hazard. Mater.*, 2023, **444**, 130301.
25 V. Gadore, S. R. Mishra and M. Ahmaruzzaman, *J. Environ. Manage.*, 2023, **334**, 117496.
26 G. Kumar, *J. Inorg. Organomet. Polym. Mater.*, 2023, **33**, 2710–2720.
27 J. Srivind, V. S. Nagarethinam, M. Suganya, S. Balamurugan, D. Prabha and A. R. Balu, *Mater. Sci. Eng. B*, 2020, **255**, 114530.
28 Q. Li, S. He, L. Wang, J. Song, J. Wang, C. Shao, Z. Tian and Y. Liu, *CrystEngComm*, 2023, **25**, 2882–2891.
29 V. Gadore, S. R. Mishra and M. Ahmaruzzaman, *Chemosphere*, 2024, **359**, 142343.
30 Y. Zhang, L. Hu, H. Zhou, H. Wang and Y. Zhang, *ACS Appl. Nano Mater.*, 2022, **5**, 391–400.
31 G. Gautam, M. Kumar and B. Singh, *Mater. Today Proc.*, 2022, **62**, 3239–3243.
32 H. Wei, Y. Zhang, Y. Zhang and Y. Zhang, *Colloids Interface Sci. Commun.*, 2021, **45**, 100550.
33 P. Salimi Kuchi, H. Roshan and M. H. Sheikhi, *J. Alloys Compd.*, 2020, **816**, 152666.
34 X. Meng, M. Bi, Q. Xiao and W. Gao, *Sens. Actuators, B*, 2022, **359**, 131612.
35 D. Gu, W. Liu, J. Wang, J. Yu, J. Zhang, B. Huang, M. N. Rumyantseva and X. Li, *Chemosensors*, 2022, **10**, 165.
36 J. Yan, Q. Li, Y. Hao, C. Dai and Y. Chen, *Funct. Mater. Lett.*, 2020, **13**, 1–4.
37 A. K. Dwivedi and S. Tripathi, *IEEE Trans. Electron Devices*, 2023, **70**, 2378–2383.
38 L. Li, Z. Wei, S. Huang, C. Li, Q. Lu and J. Ma, *J. Mater. Sci. Mater. Electron.*, 2022, **33**, 18884–18896.
39 W. Zhao, Z. Wei, X. Zhang, M. Ding and S. Huang, *Mater. Res. Bull.*, 2020, **124**, 110749.
40 T. Luttrell, S. Halpegamage, J. Tao, A. Kramer, E. Sutter and M. Batzill, *Sci. Rep.*, 2015, **4**, 4043.
41 C. S. Diko, M. Abitonze, Y. Liu, Y. Zhu and Y. Yang, *Nanomaterials*, 2022, **12**, 4497.
42 X. Guo, F. Zhang, Y. Zhang and J. Hu, *J. Mater. Chem. A*, 2023, **11**, 7331–7343.
43 L. A. Burton, T. J. Whittles, D. Hesp, W. M. Linhart, J. M. Skelton, B. Hou, R. F. Webster, G. O'Dowd, C. Reece,

D. Cherns, D. J. Fermin, T. D. Veal, V. R. Dhanak and A. Walsh, *J. Mater. Chem. A*, 2016, **4**, 1312–1318.

44 S. Mondal, S. Das and U. K. Gautam, *J. Colloid Interface Sci.*, 2021, **603**, 110–119.

45 L. Deng, H. Liu, X. Gao, X. Su and Z. Zhu, *Ceram. Int.*, 2016, **42**, 3808–3815.

46 N. Carl, M. Fiaz, H. S. Oh and Y. K. Kim, *Catalysts*, 2024, **14**, 442.

47 J. Zheng, H. Yang, F. Zheng, F. Liu, L. Lin and S. Li, *J. Phys. Chem. C*, 2022, **126**, 11629–11635.

48 J. Gao, X. Sun, L. Zheng, G. He, Y. Wang, Y. Li, Y. Liu, J. Deng, M. Liu and J. Hu, *New J. Chem.*, 2021, **45**, 16131–16142.

49 S. Ding, W. Gan, J. Guo, R. Chen, R. Liu, Z. Zhao, J. Li, M. Zhang and Z. Sun, *J. Mater. Chem. C*, 2024, **12**, 7079–7094.

50 P. Bharathi, S. Harish, M. Shimomura, M. K. Mohan, J. Archana and M. Navaneethan, *Chemosphere*, 2024, **346**, 140486.

51 Q. Sun, Y. Li, J. Hao, S. Zheng, T. Zhang, T. Wang, R. Wu, H. Fang and Y. Wang, *ACS Appl. Mater. Interfaces*, 2021, **13**, 54152–54161.

52 W. Yu, D. Chen, J. Li and Z. Zhang, *Crystals*, 2023, **13**, 1–11.

53 J. Zhang, H. Shen, Y. Li, X. Li, J. Sun, D. Yan, X. Jin and X. Wu, *Surf. Interfaces*, 2024, **54**, 105136.

54 J. Shao, X.-T. Wang, H. Xu, X.-D. Zhao, J.-M. Niu, Z.-D. Zhang, Y.-L. Huang and J.-Z. Duan, *J. Electrochem. Soc.*, 2021, **168**, 016511.

55 H. Yao and L. Liu, *Vacuum*, 2024, **222**, 113030.

56 S. Zhu, G. Wu, Z. Liu, S. Zhao, D. Cao, C. Li and G. Liu, *Ceram. Int.*, 2023, **49**, 5893–5904.

57 S. Shanmugaratnam, B. Selvaratnam, A. Baride, R. Koodali, P. Ravirajan, D. Velauthapillai and Y. Shivatharsiny, *Catalysts*, 2021, **11**, 589.

58 P. Yao, S. Yu, H. Shen, J. Yang, L. Min, Z. Yang and X. Zhu, *New J. Chem.*, 2019, **43**, 16748–16752.

59 L. Sun, Z. Zhao, S. Li, Y. Su, L. Huang, N. Shao, F. Liu, Y. Bu, H. Zhang and Z. Zhang, *ACS Appl. Nano Mater.*, 2019, **2**, 2144–2151.

60 Y. Wu, G. Lin, X. Zhou, J. Chen, J. Zhuang, Q. Chen, Y. Luo, D. Lu, V. Ganesh and R. Zeng, *J. Electroanal. Chem.*, 2020, **857**, 113740.

61 M. Kovacic, H. Kusic, M. Fanetti, U. L. Stangar, M. Valant, D. D. Dionysiou and A. L. Bozic, *Environ. Sci. Pollut. Res. Int.*, 2017, **24**, 19965–19979.

62 L. Truong-Phuoc, K. C. Christoforidis, F. Vigneron, V. Papaefthimiou, G. Decher, N. Keller and V. Keller, *ACS Appl. Mater. Interfaces*, 2016, **8**, 34438–34445.

63 J. Lin, Y. Liu, Y. Liu, C. Huang, W. Liu, X. Mi, D. Fan, F. Fan, H. Lu and X. Chen, *ChemSusChem*, 2019, **12**, 961–967.

64 K. C. Christoforidis, A. Sengele, V. Keller and N. Keller, *ACS Appl. Mater. Interfaces*, 2015, **7**, 19324–19334.

65 M. Li, H. Liu, T. Lv and M. Ding, *J. Mater. Chem. A*, 2018, **6**, 3488–3499.

66 H. She, H. Zhou, L. Li, Z. Zhao, M. Jiang, J. Huang, L. Wang and Q. Wang, *ACS Sustain. Chem. Eng.*, 2019, **7**, 650–659.

67 J. Wang, X. Li, J. Zhu, H. Li and X. Le, *Nanoscale*, 2013, **5**, 1876–1881.

68 S. Tanaka, D. Nogami, N. Tsuda and Y. Miyake, *J. Colloid Interface Sci.*, 2009, **334**, 188–194.

69 C. Rosiles-Perez, M. Ocampo Gaspar, O. J. Padilla González, L. F. Román Flores and A. E. Jiménez- González, *Emergent Mater*, 2024, **7**, 1445–1462.

70 P. Somasundaran, B. Markovic, X. Yu and S. Krishnakumar, *Handb. Surf. Colloid Chem. Second Ed.*, CRC Press, Taylor and Francis Group, London, New York, 2002, pp. 387–436.

71 P. Rana and P. Jeevanandam, *ChemNanoMat*, 2024, **10**, 1–11.

72 Profile Solar, Solar PV analysis of Roorkee, India, **https://profilesolar.com/locations/India/Roorkee/**accessed July 11, 2025.

73 A. H. Ragab, N. F. Gumaah, A. A. El Aziz Elfiky and M. F. Mubarak, *BMC Chem.*, 2024, **18**, 121.

74 L. B. Chandrasekar, R. Chandramohan, R. Vijayalakshmi and S. Chandrasekaran, *Int. Nano Lett.*, 2015, **5**, 71–75.

75 J. Madhavi, *SN Appl. Sci.*, 2019, **1**, 1–12.

76 A. Dastider, H. Saha, M. J. F. Anik, M. Jamal and M. M. Billah, *RSC Adv.*, 2024, **14**, 11677–11693.

77 M. S. Jamal, S. A. Shahahmadi, P. Chelvanathan, H. F. Alharbi, M. R. Karim, M. Ahmad Dar, M. Luqman, N. H. Alharthi, Y. S. Al-Harthi, M. Aminuzzaman, N. Asim, K. Sopian, S. K. Tiong, N. Amin and M. Akhtaruzzaman, *Results Phys.*, 2019, **14**, 102360.

78 S. Wadhai and P. Thakur, *Environ. Sci. Pollut. Res. Int.*, 2024, **31**, 60836–60851.

79 P. Praveen, G. Viruthagiri, S. Mugundan and N. Shanmugam, *Spectrochim. Acta A Mol. Biomol. Spectrosc.*, 2014, **117**, 622–629.

80 H. Liu, C. Du, H. Bai, Y. Su, D. Wei, Y. Wang, G. Liu and L. Yang, *J. Mater. Sci.*, 2018, **53**, 10743–10757.

81 Z. Wu, Y. Xue, Y. Zhang, J. Li and T. Chen, *RSC Adv.*, 2015, **5**, 24640–24648.

82 R. Gaur and P. Jeevanandam, *J. Nanosci. Nanotechnol.*, 2017, **18**, 165–177.

83 A. K. El-Sawaf, A. A. Nassar, A. A. El Aziz Elfiky and M. F. Mubarak, *Polym. Bull.*, 2024, **81**, 12451–12476.

84 S. Balu, K. Uma, G. T. Pan, T. C. K. Yang and S. K. Ramaraj, *Materials*, 2018, **11**, 1030.

85 Y. L. Pang, S. Lim and R. K. L. Lee, *Environ. Sci. Pollut. Res. Int.*, 2020, **27**, 34638–34652.

86 M. Sathish, S. Mitani, T. Tomai, A. Unemoto and I. Honma, *J. Solid State Electrochem.*, 2012, **16**, 1767–1774.

87 B. Liu, W. Wang, H. Li, Z. Jian, Y. Xing and S. Zhang, *Int. J. Electrochem. Sci.*, 2018, **13**, 6870–6879.

88 M. F. Mubarak, H. Selim, H. B. Hawash and M. Hemdan, *Environ. Sci. Pollut. Res. Int.*, 2024, **31**, 2297–2313.

89 S. Landi, I. R. Segundo, E. Freitas, M. Vasilevskiy, J. Carneiro and C. J. Tavares, *Solid State Commun.*, 2022, **341**, 1–7.

90 P. R. Jubu, E. Danladi, U. I. Ndeze, O. Adedokun, S. Landi, A. J. Haider, A. T. Adepoju, Y. Yusof, O. S. Obaseki and F. K. Yam, *Results Opt.*, 2024, **14**, 100606.

91 A. Saha, A. Moya, A. Kahnt, D. Iglesias, S. Marchesan, R. Wannemacher, M. Prato, J. J. Vilatela and D. M. Guldi, *Nanoscale*, 2017, **9**, 7911–7921.

92 C. C. Mercado, F. J. Knorr, J. L. McHale, S. M. Usmani, A. S. Ichimura and L. V. Saraf, *J. Phys. Chem. C*, 2012, **116**, 10796–10804.

93 F. J. Knorr, D. Zhang and J. L. McHale, *Langmuir*, 2007, **23**, 8686–8690.

94 D. Prabha, S. Ilangovan, J. Srivind, M. Suganya, S. Anitha, S. Balamurugan and A. R. Balu, *J. Mater. Sci. Mater. Electron.*, 2017, **28**, 15556–15564.

95 I. Iatsunskyi, M. Kempiński, G. Nowaczyk, M. Jancelewicz, M. Pavlenko, K. Załeski and S. Jurga, *Appl. Surf. Sci.*, 2015, **347**, 777–783.

96 A. K. Mohamedkhair, Q. A. Drmosh and Z. H. Yamani, *Front. Mater.*, 2019, **6**, 1–10.

97 S. Yan, K. Li, Z. Lin, H. Song, T. Jiang, J. Wu and Y. Shi, *RSC Adv.*, 2016, **6**, 32414–32421.

98 P. van der Heide, *X-Ray Photoelectron Spectroscopy: an Introduction to Principles and Practices*, John Wiley & Sons, Inc., Hoboken, New Jersey, 2011.

99 S. Jain, N. Kumar, S. Sharma, D. Parmar, R. K. Sharma, M. Tahir, K. Kumari and G. Rani, *Mater. Today Sustain.*, 2023, **24**, 100539.

100 M. Andrulevičius, S. Tamulevičius, Y. Gnatyuk, N. Vityuk, N. Smirnova and A. Eremenko, *Mater. Sci.*, 2008, **14**, 8–14.

101 L. Shi, C. Xu, X. Sun, H. Zhang, Z. Liu, X. Qu and F. Du, *J. Mater. Sci.*, 2018, **53**, 11329–11342.

102 D. M. Mwangangi, T. A. Makhetha, J. C. Ngila and L. N. Dlamini, *FlatChem*, 2025, **51**, 100865.

103 S. Ahmed, M. Ahmad, M. H. Yousaf, S. Haider, Z. Imran, S. S. Batool, I. Ahmad, M. I. Shahzad and M. Azeem, *Front. Chem.*, 2022, **10**, 1–9.

104 A. Balakrishnan, J. D. Groeneveld, S. Pokhrel and L. Mädler, *Chem.–Eur. J.*, 2021, **27**, 6390–6406.

105 J. Gajendiran and V. Rajendran, *Adv. Nat. Sci. Nanosci. Nanotechnol.*, 2011, **2**, 015001.

106 H. Zhang, T. Van Pelt, A. N. Mehta, H. Bender, I. Radu, M. Caymax, W. Vandervorst and A. Delabie, *2D Mater.*, 2018, **5**, 035006.

107 S. Samira and A. Raja P, *J. Thermodyn. Catal.*, 2012, **3**, 1–6.

108 R. K. Upadhyay, M. Sharma, D. K. Singh, S. S. Amritphale and N. Chandra, *Sep. Purif. Technol.*, 2012, **88**, 39–45.

109 G. Xing, L. Zhang, Y. Zhao, S. Li, T. Li, T. Lv, C. Yu and C. Zhao, *J. Mol. Struct.*, 2023, **1274**, 134409.

110 F. Karimi, H. R. Rajabi and L. Kavoshi, *Ultrason. Sonochem.*, 2019, **57**, 139–146.

111 S. D. Oladipo and B. Omondi, *J. Coord. Chem.*, 2022, **75**, 2170–2188.

112 M. Sharma, T. Jain, S. Singh and O. P. Pandey, *Sol. Energy*, 2012, **86**, 626–633.

113 Z. A. Piranshahi, M. Behbahani and F. Zeraatpisheh, *Appl. Organomet. Chem.*, 2018, **32**, 1–11.

114 A. Dasari and V. Guttena, *Mater. Today Commun.*, 2019, **19**, 157–169.

115 V. Manikandan, R. Elancheran, P. Revathi, P. Suganya and K. Krishnasamy, *Bull. Mater. Sci.*, 2020, **43**, 265.

116 A. K. Garg, B. Singh, S. Naskar, R. K. Prajapati, C. Dalal and S. K. Sonkar, *Langmuir*, 2023, **39**, 11036–11047.

117 A. Nezamzadeh-Ejhieh and Z. Banan, *Desalination*, 2012, **284**, 157–166.

118 V. Balchander, D. Ayodhya and R. S. Sunder, *Inorg. Chem. Commun.*, 2024, **162**, 112181.

119 R. Mohammed and M. E. M. Ali, *Environ. Nanotechnol., Monit. Manag.*, 2023, **20**, 100885.

120 G. Murugadoss, S. Salla, M. R. Kumar, N. Kandhasamy, H. Al Garalleh, M. Garaleh, K. Brindhadevi and A. Pugazhendhi, *Environ. Res.*, 2023, **220**, 115171.

121 H. Xie, T. Zeng, S. Jin, Y. Li, X. Wang, X. Sui and X. Zhao, *J. Nanosci. Nanotechnol.*, 2013, **13**, 1461–1466.

122 S. V. P. Vattikuti, I. L. Ngo and C. Byon, *Solid State Sci.*, 2016, **61**, 121–130.

123 B. S. Goud, G. Koyyada, J. H. Jung, G. R. Reddy, J. Shim, N. D. Nam and S. V. P. Vattikuti, *Int. J. Hydrogen Energy*, 2020, **45**, 18961–18975.

124 H. Fakhri, A. R. Mahjoub and A. H. C. Khavar, *Appl. Surf. Sci.*, 2014, **318**, 65–73.

125 C. Yu, K. Wang, P. Yang, S. Yang, C. Lu, Y. Song, S. Dong, J. Sun and J. Sun, *Appl. Surf. Sci.*, 2017, **420**, 233–242.

126 G. Murugadoss, S. Muruganandam, M. R. Kumar and A. Pugazhendhi, *Chemosphere*, 2023, **336**, 139100.

127 Y. Dan, J. Xu, J. Jian, L. Meng, P. Deng, J. Yan, Z. Yuan, Y. Zhang and H. Zhou, *Molecules*, 2023, **28**, 6882.

128 Q. Wei, Q. Dong, D. W. Sun and H. Pu, *Spectrochim. Acta - Part A Mol. Biomol. Spectrosc.*, 2023, **285**, 121895.

129 V. N. Nguyen, D. T. Tran, M. T. Nguyen, T. T. T. Le, M. N. Ha, M. V. Nguyen and T. D. Pham, *Res. Chem. Intermed.*, 2018, **44**, 3081–3095.

130 N. P. de Moraes, F. N. Silva, M. L. C. P. da Silva, T. M. B. Campos, G. P. Thim and L. A. Rodrigues, *Mater. Chem. Phys.*, 2018, **214**, 95–106.

131 P. Ghasemipour, M. Fattahi, B. Rasekh and F. Yazdian, *Sci. Rep.*, 2020, **10**, 4414.

132 H. J. Fan, S. T. Huang, W. H. Chung, J. L. Jan, W. Y. Lin and C. C. Chen, *J. Hazard. Mater.*, 2009, **171**, 1032–1044.

133 A. Farajollahi, A. Poursattar Marjani, N. Noroozi Pesyan and H. Alamgholiloo, *Appl. Surf. Sci.*, 2023, **622**, 156903.

134 M. Bledowski, L. Wang, A. Ramakrishnan, O. V. Khavryuchenko, V. D. Khavryuchenko, P. C. Ricci, J. Strunk, T. Cremer, C. Kolbeck and R. Beranek, *Phys. Chem. Chem. Phys.*, 2011, **13**, 21511–21519.

135 O. P. Kumar, M. N. Ashiq, M. Ahmad, S. Anjum and A. ur Rehman, *J. Mater. Sci. Mater. Electron.*, 2020, **31**, 21082–21096.

136 Q. U. Ain, U. Rasheed, M. Yaseen, H. Zhang and Z. Tong, *J. Hazard. Mater.*, 2020, **397**, 122758.

137 Z. Cao, Y. Yin, P. Fu, D. Li, Y. Zhou, Y. Deng, Y. Peng, W. Wang, W. Zhou and D. Tang, *Nanoscale Res. Lett.*, 2019, **14**, 1–9.

138 H. Wang, L. Xu, R. Zhang, Z. Ge, W. Zhang, J. Xu, Z. Ma and K. Chen, *Nanoscale Res. Lett.*, 2015, **10**, 128.

139 G. Žerjav, A. Albreht, I. Vovk and A. Pintar, *Appl. Catal. A Gen.*, 2020, **598**, 117566.

140 K. R. M. Oraby, A. Villalonga, F. S. M. Hassan, M. A. Zayed, M. F. Mubarak, I. Ojeda, A. Sánchez and R. Villalonga, *Process Biochem.*, 2025, **148**, 10–16.

141 F. Cai, X. Hu, F. Gou, Y. Chen, Y. Xu, C. Qi and D. K. Ma, *Appl. Surf. Sci.*, 2023, **611**, 155696.

142 F. Wang, S. Zhang, W. Jing, H. Qiu, Y. Liu and L. Guo, *J. Mater. Sci. Technol.*, 2024, **189**, 146–154.